A data-driven optimal control method for endoplasmic reticulum membrane compartmentalization in budding yeast cells

Aymen Laadhari, Yves Barral, Gabor Székely

A data-driven optimal control method for endoplasmic reticulum membrane compartmentalization in budding yeast cells

Aymen Laadhari[a*], Yves Barral[b], Gábor Székely[c]

[a]Department of Mathematics, Khalifa University, UAE

[b]Institute of Biochemistry, ETH Zurich, Zurich, Switzerland

[c]Department of Information Technology and Electrical Engineering, ETH Zurich, Zurich, Switzerland

[*]Corresponding author.

Abstract

In this paper, we propose a variational data assimilation approach for including data measurements in the simulation of the mobility of fluorescently labeled molecules in the yeast endoplasmic reticulum. The modeling framework aims to provide numerical evidence for compartmentalization in the endoplasmic reticulum. Experimental data is collected and an optimal control problem is formulated as a regularized inverse problem. To our knowledge, this is the first attempt to introduce an optimization formulation constrained by partial differential equations to study the kinetics of fluorescently labeled molecules in budding yeast. We derive the optimality conditions and use an Optimize-then-Discretize approach. A gradient descent algorithm allows accurate estimation of unknown key parameters in different cellular compartments. The numerical results support the empirical barrier index theory suggesting the presence of a physical diffusion barrier that compartmentalizes the endoplasmic reticulum membrane by limiting the exchange of proteins between the mother and its growing bud. We report several numerical experiments on real data and geometry, with the aim of illustrating the accuracy and efficiency of the method. Furthermore, a relationship between the size ratio of mother and bud compartments and the barrier index ratio is provided.

1 Introduction

In budding yeast cells, a small daughter cell emerges from the mother cell, which can produce nearly $20-50$ rejuvenated daughters before it dies. The endoplasmic reticulum, referred to as ER, of the budding yeast cell is made up of membranous tubules and sheet-like cisterns [Moor, 1967]. The principles underlying the anisotropic protein exchange in budding yeast have been the subject of several experimental studies showing that this is not due to the geometric organization of the ER, see [Puhka et al., 2007, Dayel et al., 1999, Lippincott-Schwartz et al., 2001, Lippencott-Schwartz et al., 2003]. The endoplasmic reticulum membrane is composed of morphologically and functionally diverse domains, such as the rough ER, the smooth ER and the nuclear envelope, whose distinction is based on the contribution of several proteins [English and Voeltz, 2013]. The membrane can be divided into large compartments roughly corresponding to future daughter cells, covering the mother compartment Γ_m which includes the nuclear envelope and is larger than the bud compartment Γ_b; The bud neck area Γ_r, however, has a sheet morphology instead of tubules [English and Voeltz, 2013], see Fig.1. In budding yeast cells as well as in a broad spectrum of eukaryotes [Caudron and Barral, 2009], experimental studies have established that the ER membrane is physically continuous throughout the cell but that a lateral diffusion barrier may exist at the level of the bud neck and compartmentalize the membrane into an anterior and a posterior domain by limiting the exchange of ER proteins between these two domains. See e.g. [Puhka et al., 2007, West et al., 2011]. From a biological point of view, the biologists suggested that the barrier could represent a specialized lipid domain in the cortical ER membrane at the bud neck with a different composition from the rest of the ER.

Studying the mobility of fluorescently tagged molecules in the ER membrane can provide biologists with important insights into the cellular function and organization. The Fluorescence Loss In Photobleaching technique, referred to as FLIP, is a fluorescence microscopy technique used in the laboratory to measure the mobility and molecular dynamics of proteins in living cells. It consists of repeatedly exposing mobile fluorescent molecules in a defined area

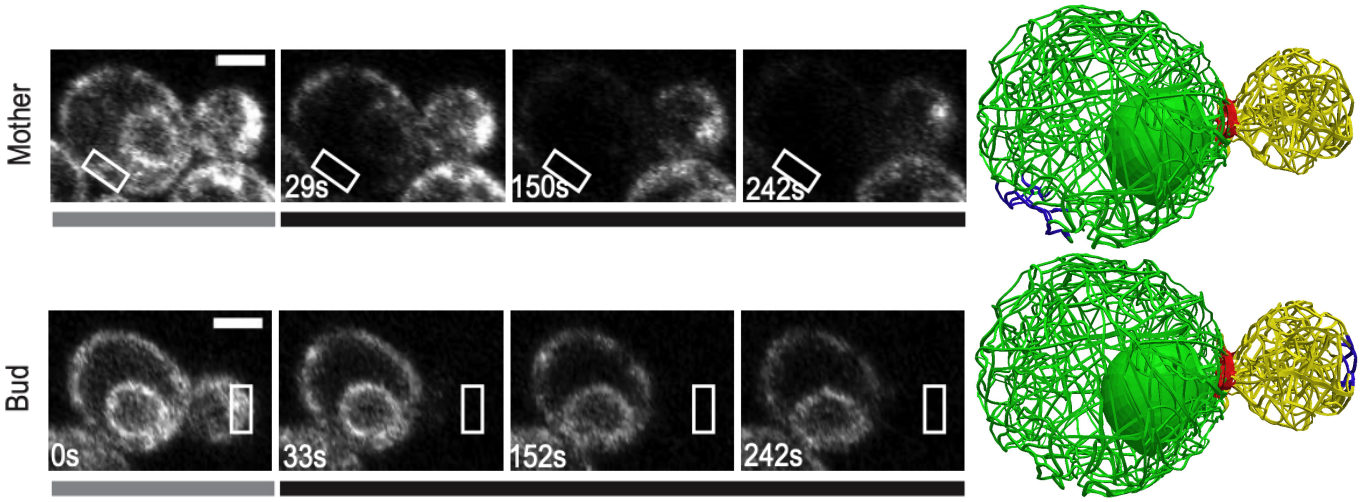

Figure 1: Confocal images of FLIP experiments applied to mother (top) or bud (bottom) domains expressing the membrane marker Sec61-GFP. The gray bars indicate the first pre-bleached images, while the black bars indicate snapshots at specific instants of repeated bleaching in the rest of the experiment. Photobleached areas are highlighted by white rectangles. (Right) Segmented geometries showing: Γ_m (green), Γ_b (yellow), Γ_r (red) and photobleached areas $\Gamma_1 \in \Gamma_m$ (top, blue) or $G_2 \in \Gamma_b$ (bottom, blue).

of interest to an intense light pulse over time by a high-intensity laser beam, thus inducing irreversible photochemical bleaching of this area, see [Clay et al., 2014, Lippencott-Schwartz et al., 2003]. Due to molecular mobility, an almost uniform decrease in fluorescence signal is observed over time throughout the membrane and is proportional to the ER protein concentration. Areas disconnected from the photobleached area should however continue to fluoresce. The rate at which fluorescence intensity changes after bleaching can provide experimenters with information about the movement of bleached molecules and the properties of surface diffusion in a particular region of a living cell. We notice that the amount of fluorescence measured after bleaching in each cell compartment is always normalized to the amount before bleaching.

Intriguingly, several experimental studies have shown that the kinetics of membrane proteins are very slow between the mother and bud compartments compared to the kinetics within each region where the rates of fluorescence loss are comparable. Indeed, applying FLIP in Γ_m results in rapid depletion of fluorescence signal in Γ_m, while fluorescence is lost only slowly in Γ_b; Conversely, applying FLIP in Γ_b leads to rapid photobleaching of the marker in Γ_b but not in Γ_m [Clay et al., 2014]. Accordingly, biologists rationalize that although the ER is physically continuous, its membrane should be compartmentalized, suggesting the presence of a barrier between the different membrane compartments, where protein diffusion is restricted somewhere [Luedeke et al., 2005].

If confirmed, this theory will have a major role in maintaining and possibly optimizing the life expectancy of nascent cells. In fact, daughter cells are born with a full life expectancy, while parent cells age after each cell division. It has been shown in the state of the art that ER stress triggers mechanisms that age yeast cells. Interestingly, compartmentalization may play a key role in retaining damage and aging factors between mothers and renewing cells by preventing the aging-causing stresses from entering the daughter cells [Tabas and Ron, 2011, Shcheprova et al., 2008, Caudron and Barral, 2009]. This remains a very thorny area of research where several elements remain unclear. To date, it remains challenging to prove and elucidate the biological relevance of such barriers. To numerically study the properties of molecular diffusion and compartmentalization on the ER membrane, we first perform several FLIP experiments in the laboratory using confocal microscopy [Clay et al., 2014]. In each FLIP experiment, we collected pointwise measurement data of the total amount of fluorescence separately in each cell compartment after photobleaching and at specific time instants. The experimental data will be used in the mathematical modeling framework detailed later. The data are also made available as supplementary material.

Numerical simulation tools based on mathematical modeling using optimal control have the potential to further investigate the aforementioned diffusion barrier theory. Optimal control problems governed by convection or convection-diffusion equations play an important role in many biomedical and engineering applications, see e.g [Douglas and Russell, 1982, Martínez et al., 2000, Zhou and Yan, 2010, Zhu and Zeng, 2003, Kim and Park, 2008, Hogea et al., 2008, Jiang and Zhang, 2000, Lenhart and Workman, 2007, Garvie and Trenchea, 2007]. Data assim-

ilation formalism represents an appropriate framework for estimating model parameters, where the problem is formulated as a PDE-constrained optimization so that the key parameters maximize a performance criterion subject to an appropriate set of constraints. An appropriate cost functional measuring the discrepancy between the numerical solutions and the experimental data is minimized, while the model parameters represent the control variables that allow the observations to be "best approximated" in some sense [Gunzburger, 2002, Liao et al., 2008]. The first-order necessary conditions for optimality, called Karush-Kuhn-Tucker conditions, enable to derive an optimality system composed by "the state problem", "the adjoint problem" and "the inversion equations". In the existing literature, Lagrange finite element discretizations of optimal control problems have been widely used in such numerical frameworks. There have been several theoretical analyzes and contributions to numerical algorithms for various applications, see e.g [Becker and Vexler, 2007, Ruo et al., 2002, Yan and Zhou, 2008, Yan and Zhou, 2009, Khaksar-E Oshagh and Shamsi, 2017, Hollis et al., 1987, Garvie and Trenchea, 2014, Casas et al., 2008, Hoppe and Neitzel, 2022, Zhou and Yan, 2010, Yücel et al., 2015]. Moreover, an extensive literature on the topic of numerical methods for the optimal control of PDEs can be found in [Betts, 2020, Mills, 1983, Kelley, 1999].

In this paper, we present a deterministic mathematical modeling framework to estimate the membrane diffusion parameters using optimal control theory and numerically explore the barrier theory in yeast cells. This is part of an ongoing work to better understand the mobility of ER proteins in different biological cells, while considering both more accurate mathematical models and uncertainty quantification in solutions. The outline of this article is as follows. In section 2, we provide the mathematical framework of the transient optimal control problem and derive first-order optimality conditions. We present in the section 3 the numerical method and the algorithm. Section 4 is devoted to the numerical experiments and exploration of the diffusion barrier theory.

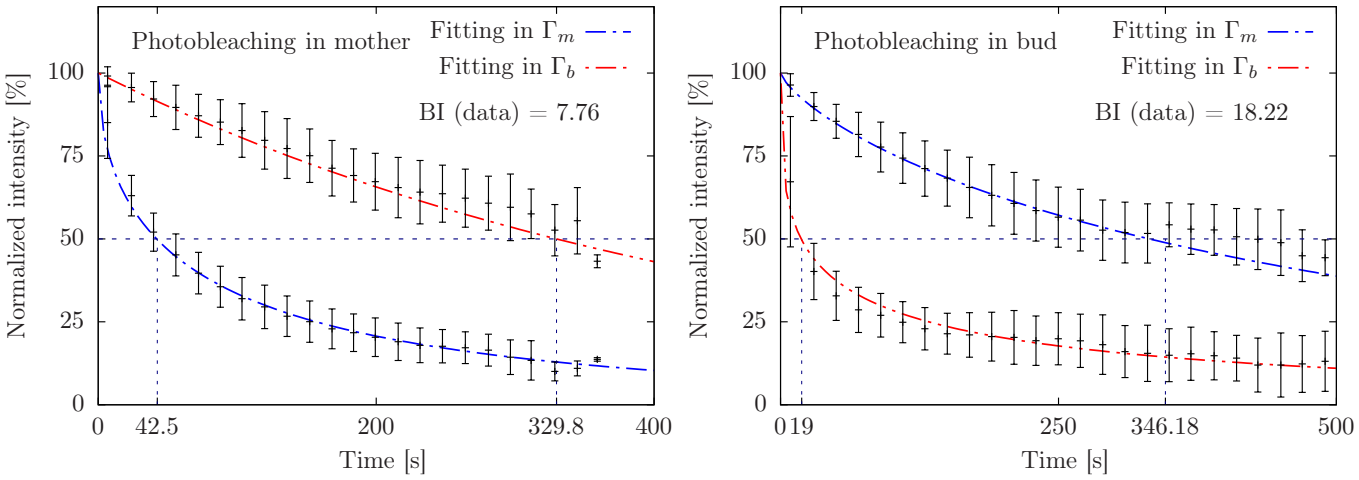

Figure 2: Experimental data showing the fluorescence signal decay over time in mother and bud compartments after an average of twenty FLIP experiments. Photobleaching is either applied to Γ_1 (left) or Γ_2 (right). Original fluorescence intensity before bleaching is set to 100% in each compartment. Mean ± SD.

2 Mathematical setting

In this section, we present the mathematical framework of the data-driven model describing the dynamics of fluorescently labeled molecules on the yeast ER membrane. The acquisition of experimental data is briefly described.

2.1 Data acquisition

A series of FLIP experiments, using time-lapse laser-scanning confocal microscopy expressing the membrane marker Sec61-GFP, allows the collection of experimental data. The experiments were performed at an ambient temperature of 23 degrees Celsius as described in [Clay et al., 2014], with some modifications as detailed in the following. Cells are imaged on the LSM 780 (Carl Zeiss, Jena, Germany) confocal microscope, while ZEN 2011 software (Carl Zeiss) is used to control the microscope. Photobleaching is applied with 100 iterations at a laser power of 100%. All intensity

values were normalized to the total cell intensity and set to the value of 100% at the start of each experiment. In each FLIP experiment, pointwise measurement data of the total amount of fluorescence are collected separately in each cell compartment after photobleaching and at specific time instants. Mean values and standard deviations (SD) are calculated from repeated experiments. Figure 1 (left) shows a budding yeast cell expressing the GFP-HDEL marker through serial optical sections, in which images were processed using the software ImageJ 1.49g (National Institutes of Health).

To investigate the diffusion barrier, fluorescence signal measurement data is collected from two different sets of FLIP experiments. In the first series of experiments, photobleaching is applied in the mother cortex on $\Gamma_1 \subset \Gamma_m$, while it is applied to the bud compartment on $\Gamma_2 \subset \Gamma_b$ in the second series of experiments, see Fig 1. Fig 2 reports the decay the amount of fluorescence signal over time in the mother and bud compartments. Each experiment was repeated on average twenty times and the error bars indicate the standard deviation of the data collected.

For the numerical computations, a realistic ER geometry, referred to as Γ, is segmented based on serial optical sections through a yeast cell. Let $\mathscr{T}_h$ be partition of Γ consisting of geometrically conforming open simplicial elements K (triangles), such that $\overline{\Gamma} = \bigcup_{K \in \mathscr{T}_h}$. Several mesh tools are used to build, improve mesh quality, and avoid badly stretched mesh elements. The initially segmented surface mesh in `STL` format is repaired and smoothed locally using MeshLab[1] and the modules for mesh optimization in Netfabb[2]. We also rely on Autodesk Maya[3] for mesh quality improvement. Finally, the unstructured triangular mesh is remeshed and optimized using the `Frontal` algorithm of Gmsh[4], see more details in [Laadhari and Székely, 2017, Laadhari and Székely, 2017]. Fig. 1 shows a segmented mesh of the ER membrane with $110'760$ triangular elements.

2.2 Direct problem

FLIP experiments have a timescale of minutes, while the most relevant dynamic process is fluorescent protein drain due to photobleaching. We assume, as in so many biological situations, that the fluorescently labeled molecules are free. Therefore, the FLIP recovery of the reporter protein reflects a dominant time-resolved pure surface diffusion scenario.

Let us consider a sufficiently smooth, orientable and closed ER surface $\Gamma \subset \mathbb{R}^3$, with an outward facing normal $\mathbf{n}$. Let $(0,T)$ represent the time period of the experiment and note $\Gamma_{i,T} = (0,T) \times \Gamma_i$ with an index $i \in \{m, b\}$. Let u_1 and u_2 be the unknown protein concentration fields on Γ at time $t \in (0,T)$ respectively for the series of FLIP experiments described above, i.e. when photobleaching is applied to G_1 and Γ_2, respectively.

The optimal control formalism allows to estimate the key parameters of the model of unknown values. Indeed, the set of control variables μ_m , μ_b and μ_r represent the surface diffusion parameters of the reporter protein respectively in the mother, bud and bud neck zones. We denote by χ_i the characteristic function which serves as an indicator of the surface Γ_i, with $i \in \{1, 2, m, r, b\}$. The total diffusion is then expressed as $\mu_{tot} = \mu_m \chi_m + \mu_b \chi_b + \mu_r \chi_r$.

Essential boundary conditions must be prescribed on $\partial\Gamma_1$ in the first set of experiments and on $\partial\Gamma_2$ when photobleaching is applied to the bud. To allow the use of the same finite element mesh in both sets of FLIP experiments and avoid further mesh manipulations on the boundaries, we consider a penalty method such as a penalty parameter $1/\varepsilon$ helps maintain zero concentration in bleached areas, see e.g. [Perić and Owen, 1992, Janela, J et al., 2005, Laadhari and Quarteroni, 2016, Astorino et al., 2012] for other applications of penalty methods. We will pay attention to the setting of the penalty parameter because a choice of too large penalty can deteriorate the conditioning of the resulting linear system and induce numerical instabilities, see for example [Laadhari and Székely, 2017].

Moreover, we assume pointwise bounds on key parameters to avoid unphysical values during the optimization process. We consider an admissible set of parameters

$$U_{ad} = \left\{ (\mu_m, \mu_b, \mu_r) \in \mathbb{R}^3 : 0 < \mu_m \leqslant A,\, 0 < \mu_b \leqslant B,\, 0 < \mu_r \leqslant C \right\},$$

where A, B and C are fixed values. Let $\mathbf{I}$ represent the identity tensor. For an arbitrary and sufficiently regular scalar function ϕ and vector $\mathbf{v}$, we introduce the surface gradient, surface divergence, and Laplace-Beltrami operators as follows:

[1] MeshLab - http://meshlab.sourceforge.net
[2] Netfabb - http://www.netfabb.com
[3] Maya - http://www.autodesk.com/products/maya
[4] Gmsh - http://www.geuz.org/gmsh

$$\begin{aligned}\boldsymbol{\nabla}_\Gamma\phi &= (\mathbf{I}-\mathbf{n}\otimes\mathbf{n})\boldsymbol{\nabla}\phi = \boldsymbol{\nabla}\phi-(\mathbf{n}.\boldsymbol{\nabla}\phi)\,\mathbf{n},\\ \mathrm{div}_\Gamma\mathbf{v} &= (\mathbf{I}-\mathbf{n}\otimes\mathbf{n}):\boldsymbol{\nabla}\mathbf{v}=\mathrm{div}\,\mathbf{v}-((\boldsymbol{\nabla}\mathbf{v})\,\mathbf{n}).\mathbf{n},\\ \Delta_\Gamma\phi &= \mathrm{div}_\Gamma\left(\boldsymbol{\nabla}_\Gamma\phi\right),\end{aligned}$$

where the tensorial product of two vectors is denoted $\otimes$, and the two times contracted product between tensors is denoted by the semicolon. They correspond to the two-dimensional operators evaluated in the tangent plane of Γ. The projector tensor $\mathbf{I}-\mathbf{n}\otimes\mathbf{n}$ has zero eigenvalue, i.e. $(\mathbf{I}-\mathbf{n}\otimes\mathbf{n})\,\mathbf{n}=\mathbf{0}$, leading to non-diffusion in the direction normal to the surface. Equipped with the initial conditions $u_{1,0}$ and $u_{2,0}$, the forward problem reads:
SP(u_1,u_2) : For given μ_m, μ_b, μ_r belonging to U_{ad}, find u_1 and u_2 such that

$$\frac{\partial u_1}{\partial t}-\mathrm{div}_\Gamma\left(\left(\mu_m\chi_m+\mu_b\chi_b+\mu_r\chi_r\right)\boldsymbol{\nabla}_\Gamma u_1\right)+\frac{1}{\varepsilon}u_1\chi_1 = 0 \quad \text{in } (0,T)\times\Gamma, \tag{2.1a}$$

$$\frac{\partial u_2}{\partial t}-\mathrm{div}_\Gamma\left(\left(\mu_m\chi_m+\mu_b\chi_b+\mu_r\chi_r\right)\boldsymbol{\nabla}_\Gamma u_2\right)+\frac{1}{\varepsilon}u_2\chi_2 = 0 \quad \text{in } (0,T)\times\Gamma, \tag{2.1b}$$

$$u_1(t=0,\cdot) = u_{1,0}(\cdot) \quad \text{in } \Gamma, \tag{2.1c}$$

$$u_2(t=0,\cdot) = u_{2,0}(\cdot) \quad \text{in } \Gamma. \tag{2.1d}$$

We use the so-called optimize-then-discretize approach rather than the discretize-then-optimize approach. Indeed, the optimality conditions will first be derived and then discretized after writing the variational formulation.

2.3 Inverse problem and parameter identification

The data collection framework provides experimental measurements of fluorescence loss kinetics separately in each cellular compartment at a discrete set of time points throughout the interval $(0,T)$, such that the averaged protein concentration in each compartment is normalized to the concentration before photobleaching. The spatiotemporal evolution of the fluorescence decay cannot be provided by the experimental setting. We first proceed with a nonlinear least-squares curve fitting of the experimental data of the total amount of fluorescence over time, as depicted in Fig. 2.

Let $F_{m,1}(t)=\exp\left(-9.71\times10^{-2}t^{0.526}\right)$ and $F_{b,1}(t)=\exp\left(-2.10\times10^{-3}t\right)$ be the time evolution functions of fluorescence loss in Γ_m and Γ_b, respectively, obtained by fitting after averaging twenty FLIP experiments in which photobleaching is applied to the mother at Γ_1. Similarly, $F_{m,2}(t)=\exp\left(-8.50\times10^{-3}t^{0.758}\right)$ and $F_{b,2}(t)=\exp\left(-2.48\times10^{-1}t^{0.352}\right)$ denote the time evolution functions of fluorescence decay in Γ_m and Γ_b, respectively, obtained by fitting after averaging twenty FLIP experiments in which photobleaching is applied at Γ_2.

The inverse problem consists in finding the optimal parameters $\mu_m^\star$, $\mu_b^\star$, and $\mu_r^\star$ such that the averaging solutions of the direct problem SP$(u_1^\star,u_2^\star)$ match as closely as possible the target averaging concentrations in each compartment. For $t\in(0,T)$, $l\in\{m,b\}$ and $i\in\{1,2\}$, and given the curve fitting functions $F_{l,i}(t)$, the optimization problem is expressed as:

$$\begin{aligned}&\textit{Find optimal parameters } (\mu_m^\star,\mu_b^\star,\mu_r^\star)=\underset{\mu_m,\mu_b,\mu_r\in U_{ad}}{\arg\inf}\ \mathcal{J}\left(u_1,u_2;\,\mu_m,\mu_b,\mu_r\right),\\ &\textit{subject to the forward problem SP (2.1a-2.1d) as a constraint.}\end{aligned} \tag{2.2}$$

The cost functional $\mathcal{J}$ is constructed by matching the temporal evolution of the average concentration predicted by the model in each cell compartment with the corresponding target experimental measurements. It depends on both the state variables and the controls and is expressed as:

$$\begin{aligned}\mathcal{J}\left(u_1,u_2;\mu_m,\mu_b,\mu_r\right) = &\sum_{i=1,2}\frac{\alpha_{m,i}}{2}\left(\int_0^T\int_{\Gamma_m}u_i(t,\boldsymbol{x})-\int_0^T F_{m,i}(t)\int_{\Gamma_m}u_{1,0}(\boldsymbol{x})\right)^2+\sum_{i=1,2}\frac{\alpha_{b,i}}{2}\left(\int_0^T\int_{\Gamma_b}u_i(t,\boldsymbol{x})-\int_0^T F_{b,i}(t)\int_{\Gamma_b}u_{2,0}(\boldsymbol{x}\right.\\ &+\sum_{i=1,2}\frac{\gamma_{m,i}}{2}\left(\int_{\Gamma_m}u_i(T,\boldsymbol{x})-F_{m,i}(T)\int_{\Gamma_m}u_{1,0}(\boldsymbol{x})\right)^2+\sum_{i=1,2}\frac{\gamma_{b,i}}{2}\left(\int_{\Gamma_b}u_i(T,\boldsymbol{x})-F_{b,i}(T)\int_{\Gamma_b}u_{2,0}(\boldsymbol{x})\right)^2\end{aligned}$$

$$+\frac{\delta}{2}\left|\mu_m-\mu_b\right|^2+\frac{\delta_m}{2}\mu_m^2+\frac{\delta_b}{2}\mu_b^2+\frac{\delta_r}{2}\mu_r^2. \tag{2.3}$$

The terms weighted by $\alpha_{\varsigma,i}$, with $\varsigma\in\{m,b\}$ and $i\in\{1,2\}$, measure the mismatch between the solution numerical and target data throughout the time interval $(0,T)$. However, the terms weighted by $\gamma_{\varsigma,i}$, with $\varsigma\in\{m,b\}$ and $i\in\{1,2\}$, measure the discrepancy at the final instant $t=T$ and lead to an optimal control with the desired states only at this instant. An appropriate choice of these weights, possibly zero, allows more emphasis to be placed on the solutions corresponding to the targets either throughout the duration of the experiment or at the end time, which can also be replaced by any other particular instant in $(0,T)$. The δ-weighted term helps account for the expectation of biologists that similar protein diffusion rates are expected in the mother and bud compartments. Finally, the terms weighted with δ_j, with $j\in\{m,b,r\}$, are the Tykhonov regularization used to cope with the possibly ill-posed character of the inverse problem in the sense of Hadamard and thwart the tendency of controls to become locally unlimited. See e.g. [Tikhonov et al., 1995, Engl et al., 2000] for a description of the mathematical theory of regularization methods. A more in-depth discussion on the choice of the regularization parameter is available in [Vogel, 2002] but is outside the scope of this work. Remark that the weights in the objective functional helps to put more emphasis on some components with respect to the other components. In practice, we either choose $\alpha_{\varsigma,i}=0$ or $\gamma_{\varsigma,i}=0$, with $\varsigma\in\{m,b\}$ and $i\in\{1,2\}$. In the sequel, the dependence on x and t will be omitted to alleviate the notations.

To derive the Karush-Kuhn-Tucker optimality conditions, we introduce the adjoint variables $v_1(t,\boldsymbol{x})$ and $v_2(t,\boldsymbol{x})$ of the corresponding state variables $u_1(t,\boldsymbol{x})$ and $u_2(t,\boldsymbol{x})$, respectively. The associated Lagrangian functional is expressed as:

$$\begin{aligned}\mathcal{L}\left(u_{i\in\{1,2\}};v_{i\in\{1,2\}};\mu_{j\in\{m,b,r\}}\right)=\ &\mathcal{J}\left(u_{i\in\{1,2\}};\mu_{j\in\{m,b,r\}}\right)\\ &-\sum_{i\in\{1,2\}}\left(\int_{\Gamma_T}\frac{\partial u_i}{dt}v_i+\int_{\Gamma_T}\left(\mu_m\chi_m+\mu_b\chi_b+\mu_r\chi_r\right)\boldsymbol{\nabla}_\Gamma u_i\cdot\boldsymbol{\nabla}_\Gamma v_i+\int_{\Gamma_T}\frac{1}{\varepsilon}\chi_i u_i v_i\right).\end{aligned} \tag{2.4}$$

The first-order optimality conditions are found by imposing the stationarity of the Lagrangian functional with respect to the adjoint, state, and inversion variables, respectively.
Let $D\mathcal{L}\left[\psi,\delta\psi\right]$ be the directional derivative of $\mathcal{L}$ at ψ along the direction $\delta\psi$. The stationarity of the Lagrangian functional with respect to the adjoint variables $D\mathcal{L}\left[v_{i\in\{1,2\}},\delta v\right]=0$ gives the direct problem SP (2.1a-2.1b). The adjoint system is obtained by imposing the stationarity of the Lagrangian functional with respect to the state variables, i.e. $D\mathcal{L}\left[u_{i\in\{1,2\}},\delta u\right]=0$. The adjoint equations read:

AP (v_1,v_2): Given the state variables u_1 and u_2 and the control variables $\mu_m,\mu_b,\mu_r\in U_{ad}$, find v_1 and v_2 such that

$$-\frac{\partial v_1}{\partial t}-\operatorname{div}_\Gamma\left(\left(\mu_m\chi_m+\mu_b\chi_b+\mu_r\chi_r\right)\boldsymbol{\nabla}_\Gamma v_1\right)+\frac{1}{\varepsilon}v_1\chi_1=\sum_{\varsigma=m,b}\sum_{j=1,2}\alpha_{\varsigma,j}\left(\int_0^T\int_{\Gamma_\varsigma}u_1-\int_0^T\int_{\Gamma_\varsigma}F_{\varsigma,j}u_{1,0}\right)\chi_\varsigma,\ \text{in } (0,T)\times\Gamma, \tag{2.5a}$$

$$-\frac{\partial v_2}{\partial t}-\operatorname{div}_\Gamma\left(\left(\mu_m\chi_m+\mu_b\chi_b+\mu_r\chi_r\right)\boldsymbol{\nabla}_\Gamma v_2\right)+\frac{1}{\varepsilon}v_2\chi_2=\sum_{\varsigma=m,b}\sum_{j=1,2}\alpha_{\varsigma,j}\left(\int_0^T\int_{\Gamma_\varsigma}u_2-\int_0^T\int_{\Gamma_\varsigma}F_{\varsigma,j}u_{2,0}\right)\chi_\varsigma,\ \text{in } (0,T)\times\Gamma, \tag{2.5b}$$

$$v_1(t=T,\cdot)=\sum_{\varsigma=m,b}\sum_{j=1,2}\gamma_{\varsigma,j}\left(\int_{\Gamma_\varsigma}u_1(T,\cdot)-F_{\varsigma,j}(T)\int_{\Gamma_\varsigma}u_{1,0}\right)\chi_\varsigma,\qquad\text{in }\Gamma, \tag{2.5c}$$

$$v_2(t=T,\cdot)=\sum_{\varsigma=m,b}\sum_{j=1,2}\gamma_{\varsigma,j}\left(\int_{\Gamma_\varsigma}u_2(T,\cdot)-F_{\varsigma,j}(T)\int_{\Gamma_\varsigma}u_{2,0}\right)\chi_\varsigma,\qquad\text{in }\Gamma, \tag{2.5d}$$

Remark that the adjoint equations (2.5a) and (2.5b) are solved backwards in time, which therefore requires terminal conditions (2.5c) and (2.5d) instead of initial conditions.

For given $a,b,x\in\mathbb{R}$, let $\pi_{[a,b]}\{x\}=\max\big(\min\left(x,b\right),a\big)$ be the projection of x on the interval $[a,b]$. By imposing the stationarity of the Lagrangian with respect to the inversion parameters, i.e. $D\mathcal{L}\left[\mu_{j\in\{m,b,r\}},\delta\mu\right]=0$, the inversion equations provide an explicit characterization of the the optimal controls as follows:

Given the state variables u_1 and u_2 and the adjoint variables v_1 and v_2, the optimal control variables read:

$$\mu_m^\star = \pi_{[0,A]}\left\{\frac{\delta_b}{\delta\delta_m+\delta_b(\delta+\delta_m)}\sum_{i=1,2}\int_0^T\int_{\Gamma_m}\boldsymbol{\nabla}_\Gamma u_i\cdot\boldsymbol{\nabla}_\Gamma v_i+\frac{\delta}{\delta\delta_m+\delta_b(\delta+\delta_m)}\sum_{\varsigma=m,b}\sum_{i=1,2}\int_0^T\int_{\Gamma_\varsigma}\boldsymbol{\nabla}_\Gamma u_i\cdot\boldsymbol{\nabla}_\Gamma v_i\right\}, \tag{2.6a}$$

$$\mu_b^\star = \pi_{[0,B]}\left\{\frac{\delta+\delta_m}{\delta}\mu_m^\star-\frac{1}{\delta}\sum_{i=1,2}\int_0^T\int_{\Gamma_m}\boldsymbol{\nabla}_\Gamma u_i\cdot\boldsymbol{\nabla}_\Gamma v_i\right\}, \tag{2.6b}$$

$$\mu_r^\star = \pi_{[0,C]}\left\{\frac{1}{\delta_r}\sum_{i=1,2}\int_0^T\int_{\Gamma_r}\boldsymbol{\nabla}_\Gamma u_i\cdot\boldsymbol{\nabla}_\Gamma v_i\right\}. \tag{2.6c}$$

From a numerical point of view, we rather opted for the use of a gradient optimization algorithm instead of an exact evaluation of the control parameters. This turned out to be more stable but requires the evaluation of the Lagrangian gradient against the control variables as detailed afterwards.

3 Numerical approximation

In this section, we describe the solution method based on a second-order time discretization and the numerical algorithm. Let us divide $[0,T]$ into $N+1$ subintervals $[t^n,t^{n+1})$, with $n=0,\cdots,N$ of constant step Δt. For any $n\geqslant 1$, we denote by u_1^n, u_2^n, v_1^n and v_2^n the approximations of u_1, u_2, v_1 and v_2 at time step n , respectively. We apply a gradient descent algorithm with an adapted step length yielding a sequence of approximations to the optimal solutions and optimal key parameters. For each iteration $k\geqslant 0$ of the gradient method, we solve the forward and inverse problems SP and AP using a fully implicit scheme.

For any $n\in[1,N+1]$ and $k>0$, the approximations of the state unknowns $u_1^{k,n}$ and $u_2^{k,n}$ are computed by induction, using values at previous time steps. Similarly, for any $n\in[0,N]$, the adjoint unknowns $v_1^{k,n}$ and $v_2^{k,n}$ are computed by induction, using values at next time steps. For $i\in\{1,2\}$, the scheme is bootstrapped by initial conditions (2.1c-2.1d) $u_i^{-1}=u_i^0=u_{i,0}$ and terminal conditions (2.5c-2.5d) $v_i^{N+2}=v_i^{N+1}=v_i(T)$, where u_i^{-1} and v_i^{N+2} only stand for convenient notations.

For each iteration k of the gradient method, the second-order backward differentiation formula, referred to as BDF2, is used for the time derivative terms. For any $n\in[0,N]$ and $k>0$, and given the control variables μ_j^k with $j\in\{m,b,r\}$, the state unknowns $u_i^{k,n+1}$ with $i\in\{1,2\}$ are computed such that

$$\int_\Gamma\frac{3u_i^{k,n+1}-4u_i^{k,n}+u_i^{k,n-1}}{2\Delta t}\xi+\int_\Gamma\left(\mu_m^k\chi_m+\mu_b^k\chi_b+\mu_r^k\chi_r\right)\boldsymbol{\nabla}_\Gamma u_i^{k,n+1}\cdot\boldsymbol{\nabla}_\Gamma\xi+\int_\Gamma\frac{1}{\varepsilon}\chi_i u_i^{k,n+1}\xi=0,\qquad\forall\xi\in H^1(\Gamma).$$

The numerical solution of the adjoint problem is computed backward in time starting from the final time $t=T$. By change of variable $\tau\equiv T-t\in(0,T)$, we obtain $\dfrac{\partial}{\partial\tau}=-\dfrac{\partial}{\partial t}$ and the terminal condition becomes an initial condition. A similar numerical scheme is used in the semi-discrete time approximation of the adjoint system. For any $n\in[1,N+1]$ and given $u_1^{k,m}$, $u_2^{k,m}$, μ_m^k, μ_b^k and μ_r^k, with $m\in[1,N+1]$, the semi-discrete adjoint problem consists in finding $v_i^{k,n-1}$ with $i\in\{1,2\}$ such that

$$\int_\Gamma\frac{3v_i^{k,n-1}-4v_i^{k,n}+v_i^{k,n+1}}{2\Delta t}\xi+\int_\Gamma\left(\mu_m^k\chi_m+\mu_b^k\chi_b+\mu_r^k\chi_r\right)\boldsymbol{\nabla}_\Gamma v_i^{k,n-1}\cdot\boldsymbol{\nabla}_\Gamma\xi+\int_\Gamma\frac{1}{\varepsilon}\chi_i v_i^{k,n-1}\xi=$$
$$\sum_{\varsigma=m,b}\sum_{j=1,2}\alpha_{\varsigma,j}\left(\int_0^T\int_{\Gamma_\varsigma}u_i^k-\int_0^T\int_{\Gamma_\varsigma}F_{\varsigma,j}u_{i,0}\right)\chi_\varsigma\xi,\qquad\forall\xi\in H^1(\Gamma).$$

Regarding the space discretization by finite elements, high order piecewise polynomial approximations using $\mathbb{P}_\kappa(K)$, with $\kappa\geqslant 1$ and $K\in\mathscr{T}_h$, are used for both state and adjoint variables.

Algorithm 1 Strategy of the optimal control problem

Set $k \leftarrow 0$, $err \leftarrow 2\epsilon_{\mathcal{J}}$
Let $(u_{1,0}, u_{2,0})$ be the known initial condition, and $\left(\mu_m^0, \mu_b^0, \mu_r^0\right)$ be the initial guess
for $n = 0, \cdots, N \equiv \dfrac{T}{\Delta t}$ **do**
  Solve SP $\left(u_1^{0,n+1}, u_2^{0,n+1}\right)$ with $u_i^{0,0} = u_{i,0}$ (initialization)
end for
Evaluate $\mathcal{J}^0$
while $err \geqslant \epsilon_{\mathcal{J}}$ **do**
  $\lambda \leftarrow 6\lambda/5$
  for $n = N+1, \cdots, 1$ **do**
    Solve AP $\left(v_1^{k,n-1}, v_2^{k,n-1}\right)$ using $u_1^{k,N+1}$ and $u_2^{k,N+1}$ for terminal conditions
  end for
  $k \leftarrow k+1$
  Compute GU $\left(\mu_m^k, \mu_b^k, \mu_r^k\right)$
  for $n = 0, \cdots, N$ **do**
    Solve SP $\left(u_1^{k,n+1}, u_2^{k,n+1}\right)$ with $u_i^{k,0} = u_{i,0}$
  end for
  Evaluate $\mathcal{J}\left(u_{i\in\{1,2\}}^k; \mu_{j\in\{m,b,r\}}^k\right)$
  while $\mathcal{J}^k > \mathcal{J}^{k-1}$ **do**
    $\lambda \leftarrow 3\lambda/4$
    if $\lambda < \epsilon_\lambda$ **then return** "Algorithm stagnated"
    end if
    Re-compute GU $\left(\mu_m^k, \mu_b^k, \mu_r^k\right)$
    for $n = 0, \cdots, N$ **do**
      Re-solve SP $\left(u_1^{k,n+1}, u_2^{k,n+1}\right)$ with $u_i^{k,0} = u_{i,0}$
    end for
    Re-evaluate $\mathcal{J}\left(u_{i\in\{1,2\}}^k; \mu_{j\in\{m,b,r\}}^k\right)$
  end while
  $err \leftarrow \dfrac{|\mathcal{J}^k - \mathcal{J}^{k-1}|}{|\mathcal{J}^{k-1}|}$
end while=0

At the computational level, we have used a gradient-based optimization algorithm because some instability issues are encountered when using an exact evaluation of the optimal controls (2.6a-2.6b-2.6c) at each optimization iteration. That requires the evaluation of the gradient of the Lagrangian with respect to the control variables. Provided with an initial guess for the controls μ_m^0, μ_b^0, and μ_r^0 and a starting value for the descent length, the control variables are updated along the gradient direction using an adapted step length λ^k as follows (3.1a-3.1b-3.1c).

GU $\left(\mu_m^k, \mu_b^k, \mu_r^k\right)$: For $k > 0$, given $\left(u_i^{k-1}, v_i^{k-1}\right)$ with $i \in \{1,2\}$ and μ_j^{k-1} with $j \in \{m, b, r\}$, compute:

$$\mu_m^k = \pi_{[0,A]}\left\{\mu_m^{k-1} - \lambda^k\left(\delta_m\mu_m^{k-1} + \delta\left(\mu_m^{k-1} - \mu_b^{k-1}\right) - \sum_{i=1,2}\int_0^T\int_{\Gamma_m}\boldsymbol{\nabla}_\Gamma u_i^{k-1}\cdot\boldsymbol{\nabla}_\Gamma v_i^{k-1}\right)\right\}, \tag{3.1a}$$

$$\mu_b^k = \pi_{[0,B]}\left\{\mu_b^{k-1} - \lambda^k\left(\delta_b\mu_b^{k-1} + \delta\left(\mu_b^{k-1} - \mu_m^{k-1}\right) - \sum_{i=1,2}\int_0^T\int_{\Gamma_b}\boldsymbol{\nabla}_\Gamma u_i^{k-1}\cdot\boldsymbol{\nabla}_\Gamma v_i^{k-1}\right)\right\}, \tag{3.1b}$$

$$\mu_r^k = \pi_{[0,C]}\left\{\mu_r^{k-1} - \lambda^k\left(\delta_r\mu_r^{k-1} - \sum_{i=1,2}\int_0^T\int_{\Gamma_r}\boldsymbol{\nabla}_\Gamma u_i^{k-1}\cdot\boldsymbol{\nabla}_\Gamma v_i^{k-1}\right)\right\}. \tag{3.1c}$$

We proceed with an adaptation strategy for the step length λ^k to ensure the decrease of the cost functional. Indeed, the step length is rejected and therefore decreased in the case where the cost functional does not decrease.

Control variables are updated only if the step length is accepted, while we exit the algorithm if λ drops below a threshold value ϵ_λ. The gradient descent iterations are repeated until the relative change in the cost functional becomes smaller than a given tolerance $\epsilon_\mathcal{J}$. Hence, convergence is achieved at iteration $k > 0$ if

$$err \equiv \frac{\left|\mathcal{J}^k - \mathcal{J}^{k-1}\right|}{\left|\mathcal{J}^{k-1}\right|} < \epsilon_\mathcal{J}, \qquad \text{with } \mathcal{J}^k \equiv \mathcal{J}\left(u^k_{i\in\{1,2\}}; \mu^k_{j\in\{m,b,r\}}\right).$$

The pseudo-code of the overall iterative scheme is detailed in Algorithm 1.

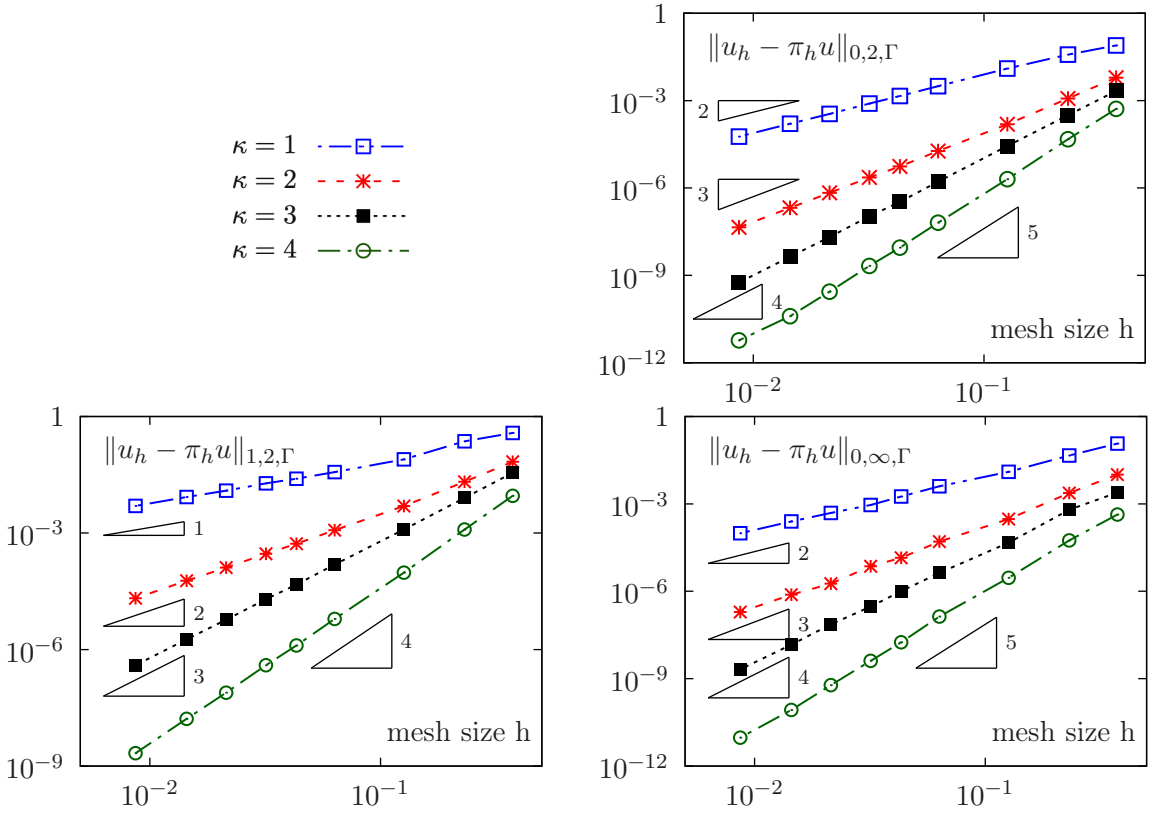

Figure 3: Example 1: Study of the spatial convergence in the norms $L^2(\Gamma)$ (top), $H^1(\Gamma)$ (bottom left) and $L^\infty(\Gamma)$ (bottom right) for high order Lagrange polynomials $\mathbb{P}_\kappa$ and high order curved surface meshes. The logarithmic scale is used.

4 Numerical results

The method has been implemented using Rheolef [Saramito, 2020], which represents a C++ library for scientific computing with special emphasis on finite elements. The parallel computing relies on MPI[5] and MUMPS which is used for factorization and as direct solver on distributed-memory architectures. Rheolef relies also on the libraries Boost[6], Blas[7], Scotch[8], and UMFPACK[9] for much of its functionalities. Numerical results are visualized graphically using the open source application Paraview[10] and Gnuplot[11]. The computations are performed on a workstation with an Intel ® Core ™ i7-4790 (3.6 GHz) processor.

[5]Message Passing Interface - http://www.mpich.org
[6]Boost libraries - http://www.boost.org
[7]Basic Linear Algebra Subprograms library - http://www.netlib.org/blas
[8]Scotch - http://www.labri.fr/perso/pelegrin/scotch
[9]Umfpack routines - http://www.cise.ufl.edu/research/sparse/umfpack/
[10]Paraview - http://www.paraview.org
[11]Gnuplot - http://www.gnuplot.info

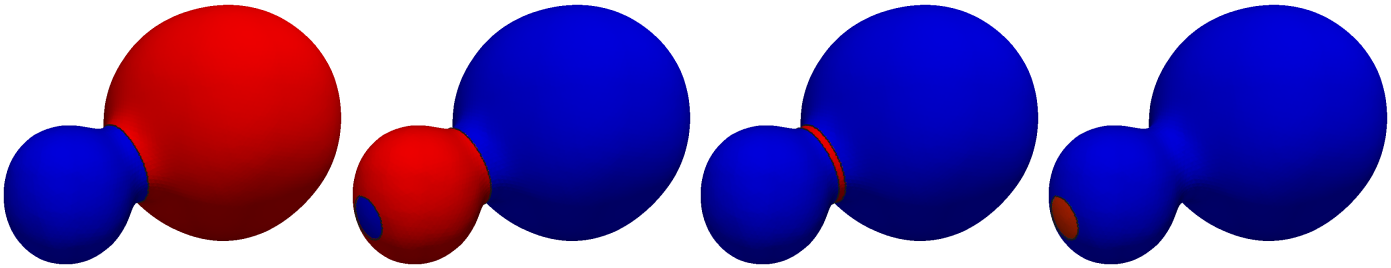

Figure 4: Example 2: Idealized and simplified geometry of yeast ER highlighting in red the mother, bud, bud neck and photobleaching areas, respectively.

In the following, we provide a set of numerical examples to evaluate the performance of the presented numerical method, with the ultimate goal of investigating numerically the barrier index theory.

4.1 Example 1

The purpose of this example is to validate the accuracy of the resolution of the direct problem, mainly the assembly of surface operators for the numerical solutions of elliptic surface partial differential equations. We consider a test case presented in [Deckelnick et al., 2010] and study numerically the convergence properties of the solution.The problem consists in solving:

$$u - \Delta_\Gamma u = \alpha \left(3x^2y - y^3\right) \quad \text{in } \Gamma, \qquad \text{with } \alpha = -\frac{13}{8}\sqrt{\frac{35}{\pi}}.$$

The geometry is the unit sphere $\left\{\boldsymbol{x} \in \mathbb{R}^3 : |\boldsymbol{x}| = 1\right\}$ and the exact solution is given by:

$$u(\boldsymbol{x}) = \alpha \frac{|\boldsymbol{x}|^2}{12 + |\boldsymbol{x}|^2} \left(3x^2y - y^3\right).$$

We study the spatial accuracy for high order finite element approximations by computing the error in the norms $L^2(\Gamma)$, $H^1(\Gamma)$ and $L^\infty(\Gamma)$ of the computed solution u_h on successively refined meshes with respect to the reference exact solution $\pi_h u$, where π_h is the Lagrange interpolation operator in the corresponding finite element space.

The decrease in errors with respect to mesh size and convergence rates are shown in Fig. 3. Results depict the conformity between numerical and exact solutions for several polynomial finite element approximations. For

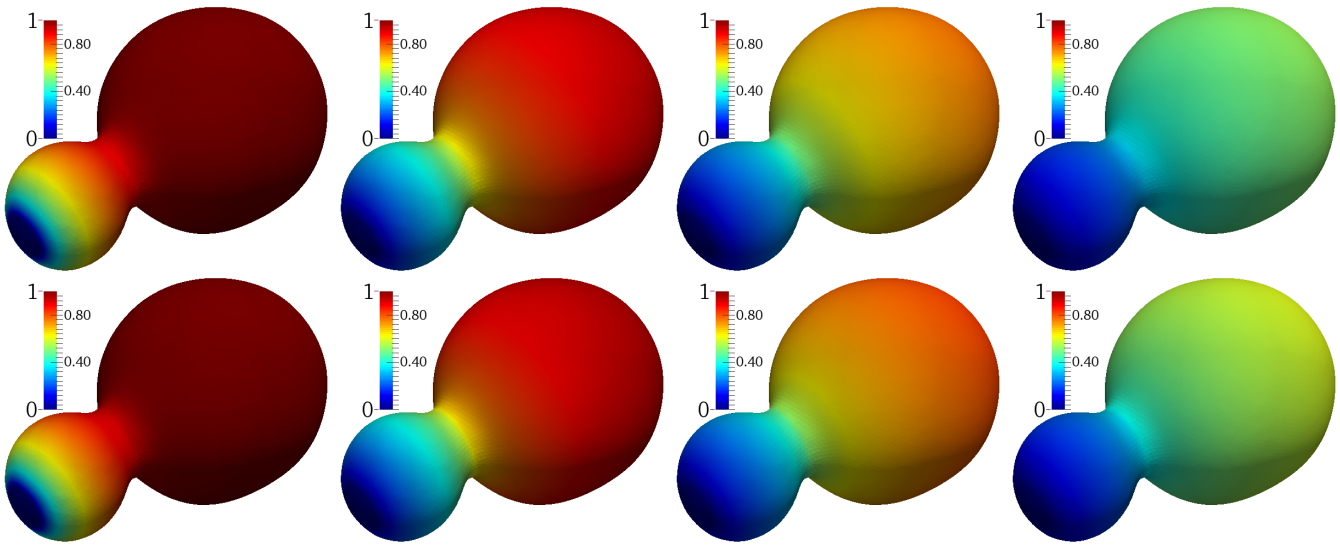

Figure 5: Example 2: Snapshots showing the computed fluorescence loss kinetics at optimal state for times $t \in \{10, 70, 170, 340\}$ with a mesh $h = 4 \times 10^{-3}$. Top: $\alpha_{m,2} = \alpha_{b,2} = 2 \times 10^4$, $\gamma_{m,2} = \gamma_{b,2} = 0$. Bottom: $\alpha_{m,2} = \alpha_{b,2} = 0$, $\gamma_{m,2} = \gamma_{b,2} = 10^8$.

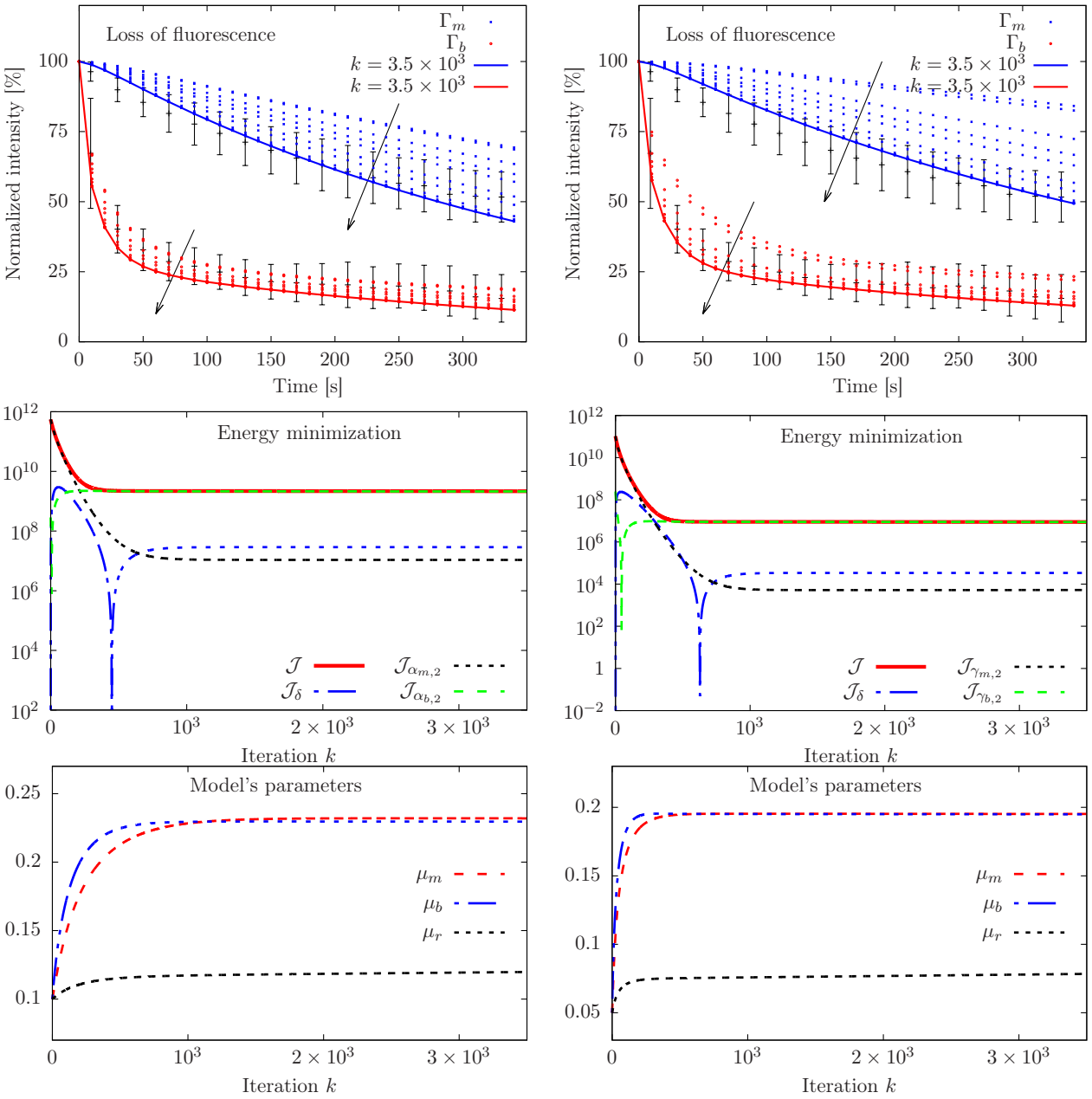

Figure 6: Example 2: Numerical results of the optimal control with the desired states enforced over the entire time period (Left: $\gamma_{m,2} = \gamma_{b,2} = 0$) and with the desired states at the final time T (Right: $\alpha_{m,2} = \alpha_{b,2} = 0$). Top: Loss of fluorescence over time at certain iterations towards convergence. The arrows show the convergence towards the optimal control solution for certain values of k between 0 and 3500. Center: Minimization of the functional cost. Bottom: Convergence of key model parameters.

example, for the Lagrange polynomials $\mathbb{P}_3$, the experimental order of convergence is 4 in the norm $L^2(\Gamma)$, whereas it is equal to 3 in the $H^1(\Gamma)$ norm. The results matches the theoretical error estimates $\|u_h - \pi_h u\|_{0,2,\Gamma} < Ch^{\kappa+1}$ and $\|u_h - \pi_h u\|_{1,2,\Gamma} < Ch^{\kappa}$, where C represents a constant, $h = \max_{K \in \mathcal{T}_h} \text{diameter}(K)$ represents the mesh size, and κ is the degree of the polynomial approximation with $\kappa \in \{1, 2, 3, 4\}$, see [Deckelnick et al., 2010].

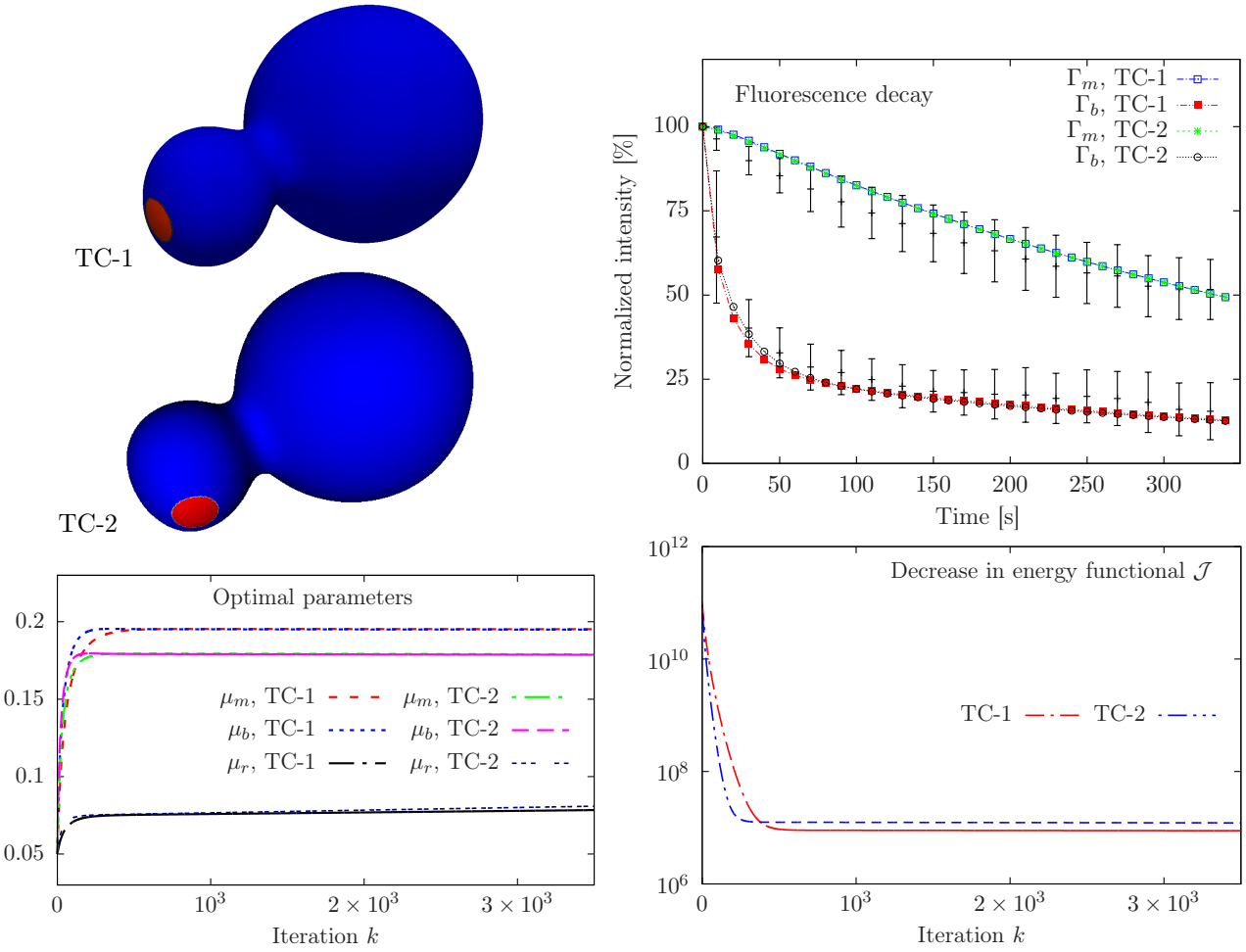

Figure 7: Example 2: Test cases, referred to as TC-1 and TC-2, with different photobleaching areas colored in red (top left). Time evolution of the fluorescence decay (top right). Change in optimal parameters (bottom left) and energy decay (bottom right).

4.2 Example 2: Optimal control simulations in simplified geometry

In this example, we proceed with a numerical validation of the proposed method in the case of simplified geometry and data. We consider an idealized geometry encompassing the convex envelopes of the mother and bud domains, and we generate successively refined semi-regular meshes. Photobleaching is only applied to the bud domain and we consider the corresponding set of experimental measurements of fluorescence loss. The different subdomains are described as regularized Heaviside functions (see for example [Laadhari, 2018b, Laadhari, 2017, Laadhari, 2018a]), and are highlighted in Fig. 4. Thus, the direct problem consists in finding u_2 satisfying (2.1b-2.1d), with $\alpha_{m,1} = \alpha_{b,1} = \gamma_{m,1} = \gamma_{b,1} = 0$ in (2.3).

To test the robustness of the method for different choices of the energy parameters, we consider two different sets of parameters so that we minimize the difference between the solution and the targets either over the whole time interval or at the final instant, respectively. In the first experiment, we consider $h = 0.043$, $\varepsilon = 10^{-10}$, $\mathbb{P}_1$ Lagrange polynomials, $\alpha_{m,2} = \alpha_{b,2} = 2 \times 10^4$, $\gamma_{m,2} = \gamma_{b,2} = 0$, $\delta = 10^{13}$, $\delta_m = \delta_b = \delta_r = 1$, and $\mu_m^0 = \mu_b^0 = \mu_r^0 = 0.1$. For the optimal control with desired states at the final time, we choose $h = 0.043$, $\varepsilon = 10^{-10}$, $\mathbb{P}_1$ Lagrange polynomials, $\alpha_{m,2} = \alpha_{b,2} = 0$, $\gamma_{m,2} = \gamma_{b,2} = 10^8$, $\delta = 10^{12}$, $\delta_m = \delta_b = \delta_r = 1$, and $\mu_m^0 = \mu_b^0 = \mu_r^0 = 0.05$. We run the simulations for $t \in (0, T = 349)$ until the convergence of the optimal control algorithm is reached. The time evolution of fluorescence loss kinetics is displayed in Fig. 6 (top) for several values of k, showing a slightly different kinetics as the matching with the data is enforced in different ways. In Fig. 6 (top right), the iterative procedure converges and allows estimating the optimal parameters so that the solution corresponds to the target kinetics at $t = T$. In Fig. 6 (center), we plot using a semi-logarithmic scale the decrease of the cost functional as a function of the number of

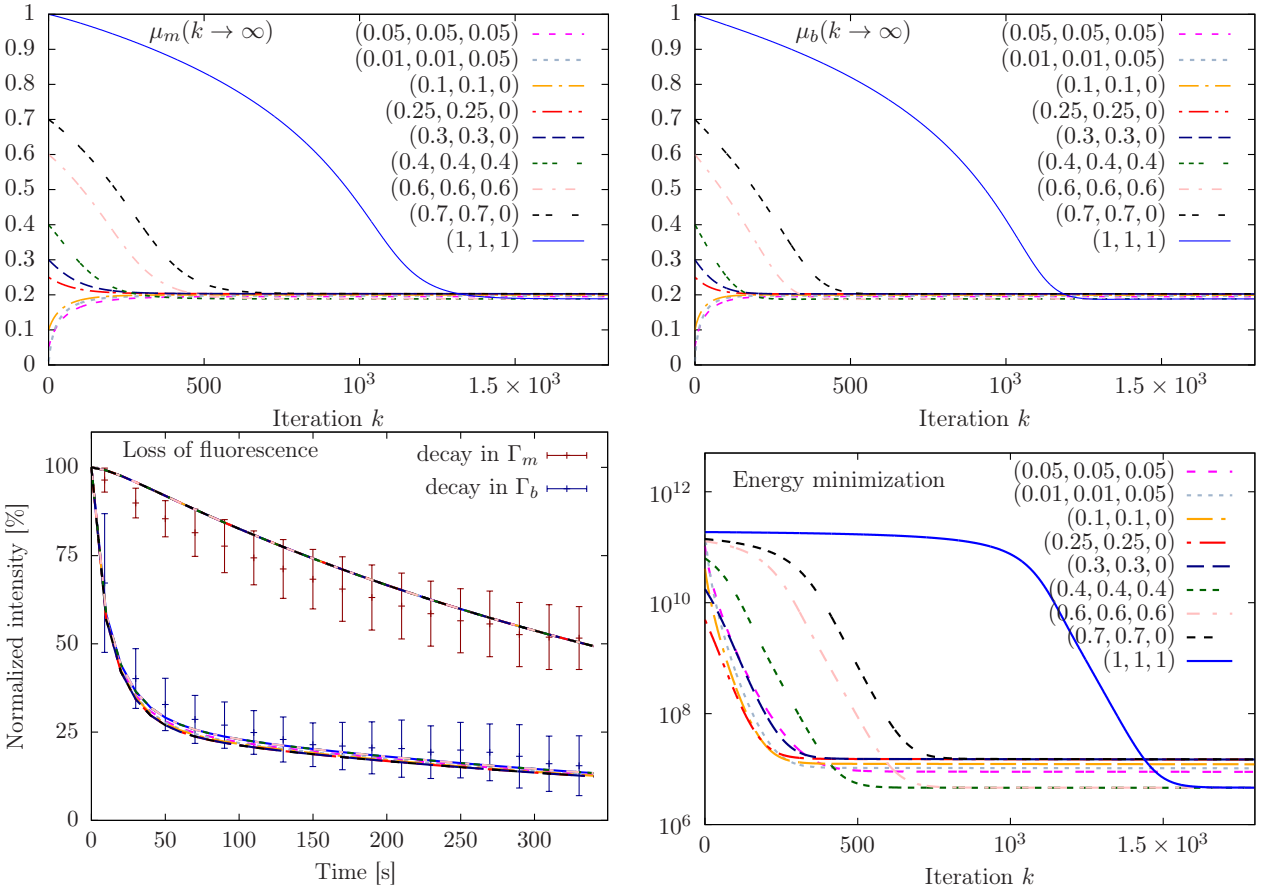

Figure 8: Example 2: Modification of estimates of control variables and optimal control solution for different choices of starting values for key parameters. Simulation parameters: $\alpha_{m,2} = \alpha_{b,2} = 0$, $\gamma_{m,2} = \gamma_{b,2} = 10^8$, $\delta = 10^{12}$, $\delta_m = \delta_b = \delta_r = 1$.

iterations for the two experiments, where $\mathcal{J}_\delta$ represents the energy term weighted by δ in (2.3) (similarly for the other energy terms). We observe a first phase characterized by a rapid decrease is followed by a plateau characterizing convergence, where the optimal objective values are respectively 2.17×10^9 and 8.83×10^6. We can also verify that the control parameters converge in Fig. 6 (bottom), showing a rapid increase from the starting values followed by a plateau characterized by $\mu_m \approx \mu_b$. The estimated optimal key parameters are $\mu_m = 0.232, \mu_b = 0.229, \mu_r = 0.124$ in the first test case, while $\mu_m = 0.195, \mu_b = 0.195, \mu_r = 0.078$ in the second case. Using the optimal parameters found, Fig. 5 provides snapshots of the numerical solution at the same times for the two aforementioned cases.

Sensitivity of the optimal control solution to the photobleaching area: We now study the sensitivity of the optimal control solution to the change in the photobleaching area in the same compartment Γ_b. We consider two test cases with different photobleaching areas as shown in Fig. 7. We consider a mesh size $h = 0.043$ and use $\mathbb{P}_1$ Lagrange polynomials. The cost function parameters are set as follows: $\alpha_{m,2} = \alpha_{b,2} = 0$, $\gamma_{m,2} = \gamma_{b,2} = 10^8$, $\delta = 10^{12}$, $\delta_m = \delta_b = \delta_r = 1$. Fig. 7 (top left) shows similar kinetics of fluorescence decay at convergence. Energy is minimized and convergence is achieved. The optimal model parameters are slightly different at convergence since the photobleaching is applied to different areas in Γ_b. Nevertheless, we notice that we continue to have almost identical values of μ_m and μ_b at the optimal state in each experiment, which remains significantly higher than the diffusion parameter at the bud neck Γ_r, as will be subsequently discussed.

Sensitivity of the optimal control solution to the initial guesses: We now investigate the sensitivity of the optimal control solution to the choice of starting values of the key parameters μ_m, μ_b and μ_r. We run the simulations

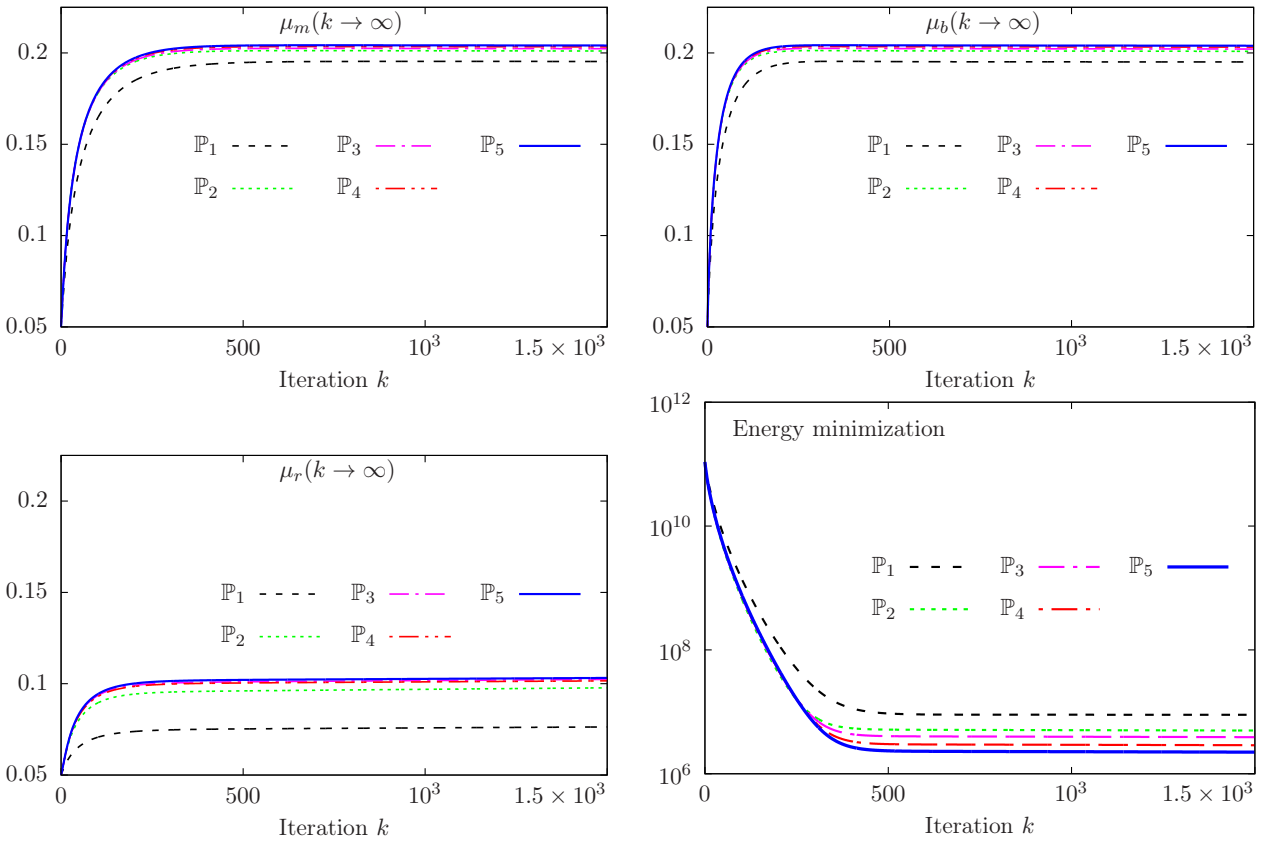

Figure 9: Example 2: Change in the estimates of control variables and cost functional for high order finite elements. Parameters: $\alpha_{m,2} = \alpha_{b,2} = 0$, $\gamma_{m,2} = \gamma_{b,2} = 10^8$, $\delta = 10^{12}$, $\delta_m = \delta_b = \delta_r = 1$ and $\mu_m^0 = \mu_b^0 = \mu_r^0 = 0.05$.

for $h = 0.043$ using $\mathbb{P}_1$ Lagrange polynomials. The cost functional parameters are set as follows: $\alpha_{m,2} = \alpha_{b,2} = 0$, $\gamma_{m,2} = \gamma_{b,2} = 10^8$, $delta = 10^{12}$, $\delta_m = \delta_b = \delta_r = 1$ so that more emphasis is placed on the solution matching targets at instant $t = T$. For different choices of the starting values, Fig. 8 plots the changes in μ_m, μ_b, the objective functional $\mathcal{J}$ and the loss of fluorescence in Γ_m and Γ_b, showing that the optimal control solution is relatively insensitive to changes in the initial guesses. As expected, choosing a relatively far initialization of the model parameters results in slower convergence to the desired state. Indeed, convergence is reached after 250 iterations for $\mu_m^0 = \mu_b^0 = \mu_r^0 = 0.05$, whereas it is reached after 1500 iterations for $\mu_m^0 = \mu_b^0 = \mu_r^0 = 1$.

Convergence study for high order piecewise finite element approximations: In this test case, we study the sensitivity of the optimal parameters to the choice of the finite element approximation. We run the simulations searching for solutions in spaces generated by Lagrange polynomials of higher order $\mathbb{P}_\kappa, \kappa \geqslant 1$. We study the estimated optimal solutions with respect to the total number of degrees of freedom, referred to as Dof, for a fixed number of mesh elements.

$\mathbb{P}_\kappa$	Dof	$\mu_m^\star$	$\mu_b^\star$	$\mu_r^\star$	$\mathcal{J}^\star$
$\mathbb{P}_1$	2407	0.195178	0.194918	0.0784062	8.83096E+6
$\mathbb{P}_2$	9622	0.201067	0.200895	0.0977545	4.98737E+6
$\mathbb{P}_3$	21647	0.202328	0.202163	0.102388	3.89932E+6
$\mathbb{P}_4$	38492	0.203342	0.203204	0.101571	2.89142E+6
$\mathbb{P}_5$	60127	0.204080	0.203959	0.103173	2.23366E+6
Reference values		0.206645	0.206725	0.102447	1.51009E+6

Table 1: Example 2: Convergence history for high order finite element approximations using $\mathbb{P}_\kappa$ with $\kappa \geqslant 1$.

We consider the following parameters: $\alpha_{m,2} = \alpha_{b,2} = 0$, $\gamma_{m,2} = \gamma_{b,2} = 10^8$, $\delta = 10^{12}$ and $\delta_m = \delta_b = \delta_r = 1$. The time step size is chosen small enough not to influence substantially the overall accuracy. The time horizon is $(0, T = 349)$. The evolution of the model parameters and the evolution of the energy cost with respect to the number of iterations are provided in Fig. 9, showing an overall convergence for higher degrees. Table 1 reports the optimal quantities calculated at convergence, i.e. when $k \to \infty$, for higher polynomial degrees as well as the corresponding reference values, obtained by numerical continuation.

Spatial convergence study: Hereafter, we carry out a quantitative convergence study with respect to the reference solution $q_{\mathrm{t,ref}}$ obtained by fitting the available measurement data. Let NTS design the number of time steps in each numerical simulation. We introduce the relative error corresponding to the temporal evolution of the quantity q_t and its rate of convergence as follows:

$$\|e_h\|_{\Gamma_b,2} = \left(\sum_{t=1}^{\mathrm{NTS}} |q_{\mathrm{t,ref}} - q_{\mathrm{t},h}|^2 \right)^{1/2}, \quad \text{with} \quad q_t = \int_{\Gamma_b} u_2(t, \boldsymbol{x}) \, \mathrm{d}\boldsymbol{x} \quad \text{and} \quad \mathrm{ROC} = \frac{\log_{10}\left(\|e_h\|_{\Gamma_b,2}\right)}{\log_{10}(h)}.$$

The parameter h represents an average mesh size within a given mesh refinement level, while $q_{\mathrm{t},h}$ is an approximation of q_t using $\mathscr{T}_h$. For different values of NTS, we appropriately consider the standard linear interpolation applied to the solution q_t. The results in Table 2 show that the aforementioned quantity converges with a more than linear order of convergence in the l_2-norm.

h	Dof	$\mu_m^\star(k \to \infty)$	$\mu_b^\star(k \to \infty)$	$\mu_r^\star(k \to \infty)$	ROC
0.094	1450	0.17493	0.17427	0.07649	2.77
0.060	2634	0.18637	0.18594	0.06838	2.33
0.043	4810	0.19538	0.19512	0.07592	2.08
0.038	7262	0.19930	0.19912	0.07714	1.85
0.029	12556	0.20756	0.20755	0.08490	1.65
0.019	26692	0.21499	0.21509	0.09372	1.53
0.014	28348	0.21669	0.21682	0.09342	1.53
0.009	102084	0.22317	0.22343	0.10016	1.37
0.007	150522	0.22501	0.22531	0.10168	1.31
0.004	368908	0.22799	0.22836	0.10386	1.19
Reference values		0.2305	0.2309	0.1084	–

Table 2: Example 3: Convergence history of same outputs with respect to spatial resolution. Simulation parameters: $\mathbb{P}_1$ Lagrange polynomials, $\alpha_{m,2} = \alpha_{b,2} = 0$, $\gamma_{m,2} = \gamma_{b,2} = 10^8$, $\delta = 10^{12}$, $\delta_m = \delta_b = \delta_r = 1$, and $\mu_m^0 = \mu_b^0 = \mu_r^0 = 0.05$.

Computational cost: To study the computational features of the proposed optimal control strategy for different choices of energy parameters, we run two different simulations with the same spatial resolution $h = 0.014$ using the $\mathbb{P}_1$ Lagrange polynomials. We choose the parameters $\alpha_{\varsigma,2} = 2 \times 10^4$, $\gamma_{\varsigma,2} = 0$, $\delta = 10^{13}$, $\delta_m = \delta_b = \delta_r = 1$ in the first simulation, while we set $\alpha_{\varsigma,2} = 0$, $\gamma_{\varsigma,2} = 10^8$, $\delta = 10^{12}$, $\delta_m = \delta_b = \delta_r = 1$, with $\varsigma \in \{m, b\}$, in the second simulation. Parallel calculations are performed until convergence on a workstation using 4 cores. The computational cost is 749.4 s in the first case, while it is 636.2 s in the second case, which shows that the prescription of the matching at the final instant presents lower but not significant computational savings compared to the case where matching is imposed in the entire time interval. However, it should be noted that the two choices of energy parameter lead to qualitatively similar results in terms of fluorescence kinetics and ratios between the optimal parameters at convergence, as show above in Fig. 6. Therefore, the choice $\alpha_{\varsigma,i} = 0$ will be preferred in the sequel.

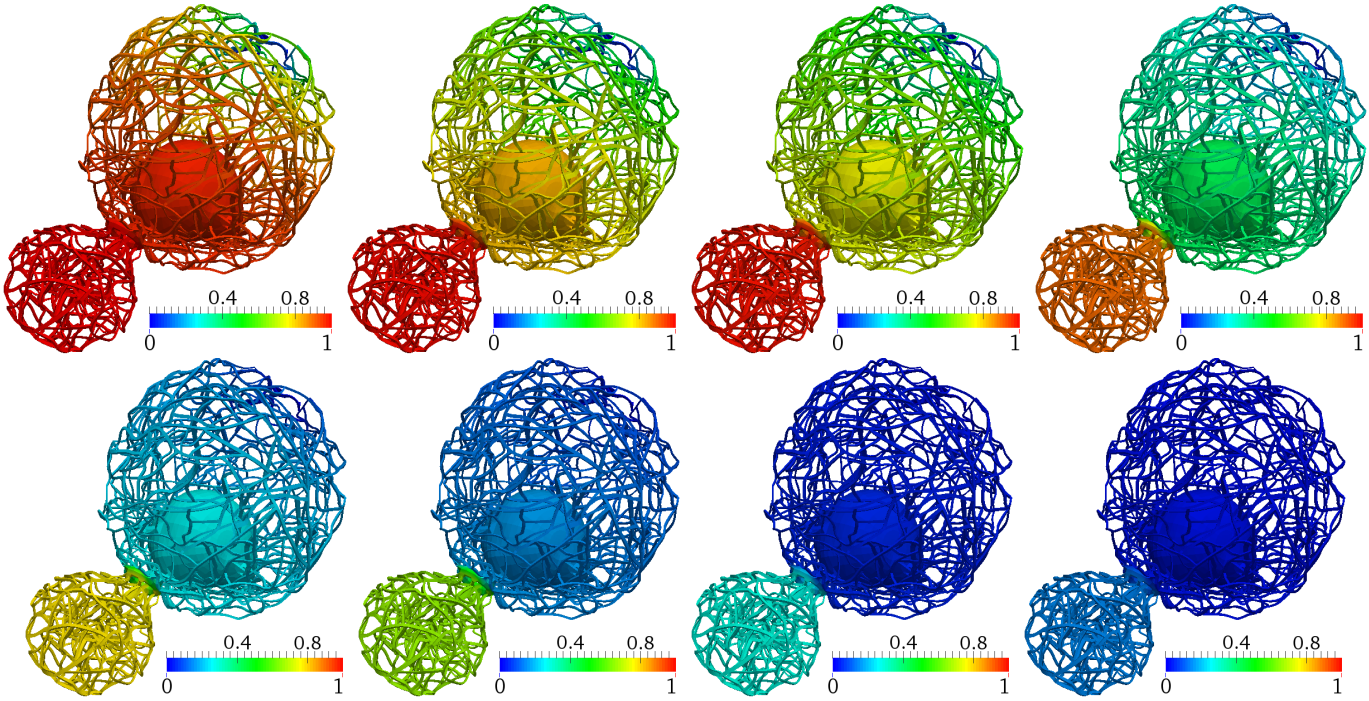

Figure 10: Example 3: Flipping in mother compartment. Snapshots showing fluorescence kinetics loss in numerical simulations with optimal model's parameters at times $t \in \{5, 15, 20, 50, 80, 110, 250, 355\}$.

4.3 Example 3: Diffusion barrier in yeast endoplasmic reticulum

Hereinafter, we focus exclusively on the numerical investigation of the empirical conclusions of compartmentalization by diffusion barrier, where the optimization is performed over the time interval of each FLIP experiment. We run numerical simulations using the data-driven model to investigate key model parameters in different cellular compartments, paying particular attention to the change in the cost functional. However, the effect of compartment size ratio on the kinetics of fluorescence will be subsequently explored in Example 4.4.

In this regard, we consider the setting and measurements of the aforementioned series of FLIP experiments described in subsection 2.1, where photobleaching is applied either at the mother or bud compartments. A unstructured realistic ER mesh of nearly regular triangular elements is considered. The initial guess of the key parameters to be estimated iteratively is $\mu_m^0 = \mu_b^0 = \mu_r^0 = 0.43$, while we choose $\varepsilon = 10^{-10}$ and $\delta_m = \delta_b = \delta_r = 1$.

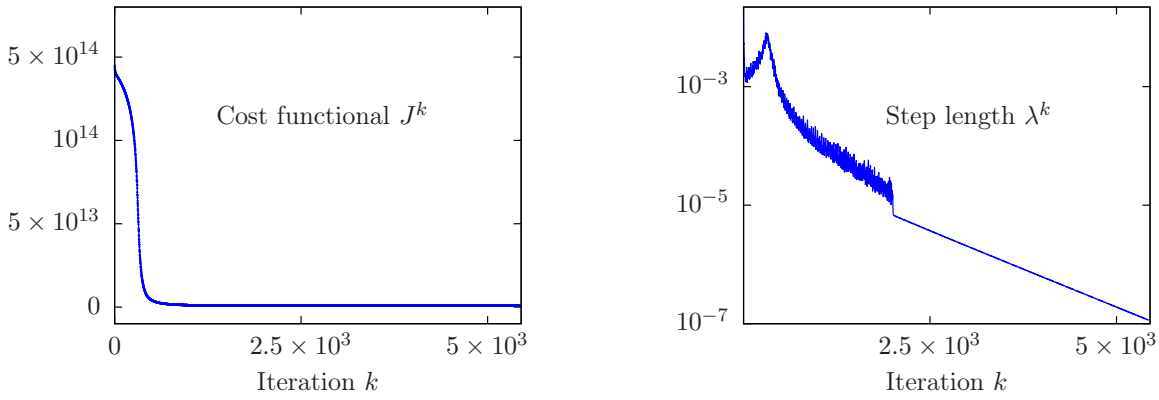

Figure 11: Example 3: (Left) Convergence of the objective functional with respect to the iterations count k. (Right) Change in the step length with respect to the iteration count. The logarithmic scale is used on the y axis. Parameters: $\delta = 10^6$, $\alpha_{\varsigma,j} = 10^6$ and $\gamma_{\varsigma,j} = 0$ for $\varsigma \in \{m, b\}$ and $j \in \{1, 2\}$, and $\delta_m = \delta_b = \delta_r = 1$.

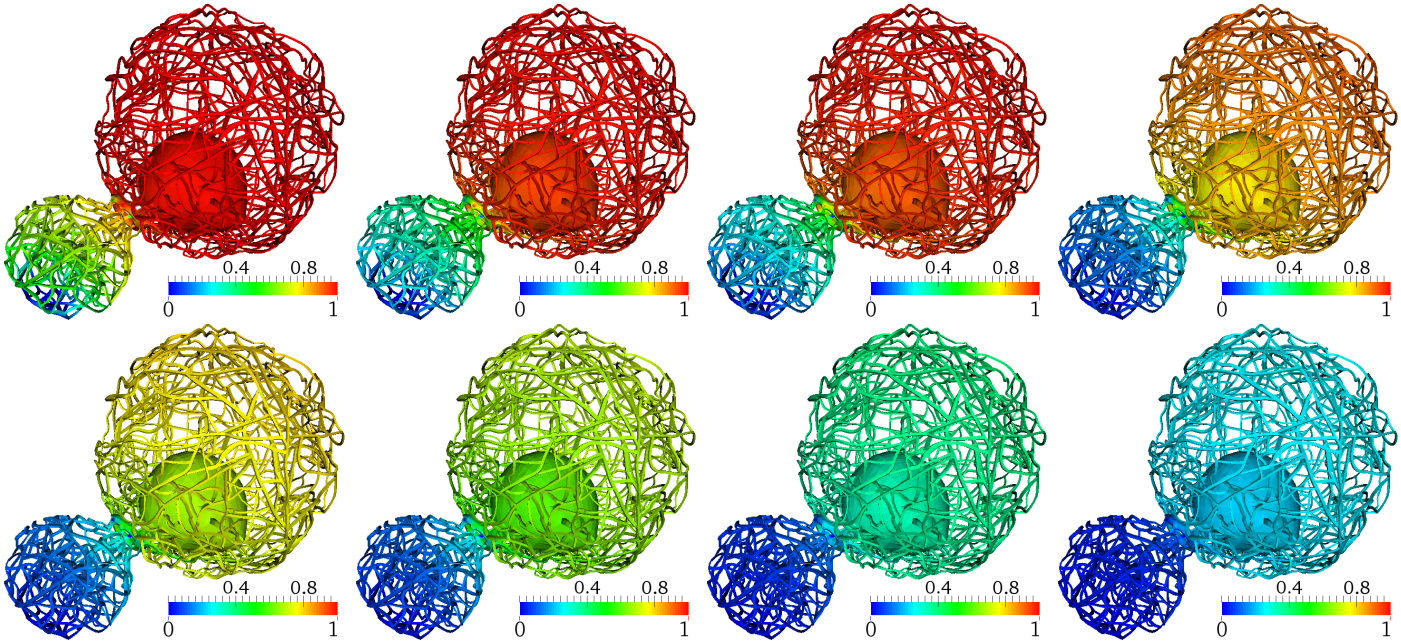

Figure 12: Example 3: Flipping in bud compartment. Snapshots showing fluorescence kinetics loss in numerical simulations with optimal model's parameters at times $t \in \{5, 15, 20, 50, 80, 110, 250, 355\}$.

The optimal control algorithm provided satisfactory results illustrating the convergence of the iterative procedure. Moreover, we follow the decay of the objective functional $\mathcal{J}^k$ with respect to the number of descent gradient iterations in Fig. 11 (left). The graph shows a rapid decrease in cost in an initial phase, followed by a horizontal plateau reached when the minimum is reached; That corresponds to the optimal objective functional obtained with the estimated optimal parameters.

The evolution of the adapted step length λ^k with respect to the number of iterations is reported in Fig. 11 (right). It shows in a first phase several fluctuations due to the adaptation of the step length to ensure the decrease of the cost functional, featuring here a rapid decrease. The variations of $\mathcal{J}$ are small thereafter, leading to lower and lower values of λ^k until it becomes lower than the tolerance threshold ϵ_λ when convergence is reached.

The change of model parameters with respect to the number of iterations is provided in Fig. 13. At convergence, the estimated model parameters are $\mu_m^\star = 0.661853$, $\mu_b^\star = 0.661895$ and $\mu_r^\star = 0.0312565$. The direct problem is then solved for both FLIP experiments using the estimated optimal parameters. We evaluate the normalized intensity values throughout the time periods in both bleached and unbleached cell compartments. Fig. 14 shows the target

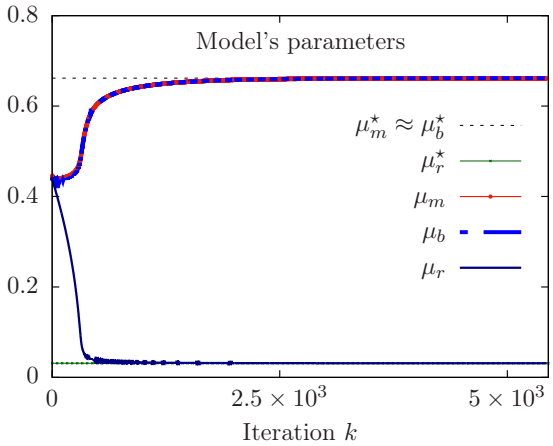

Figure 13: Example 3: Change in the estimates of control variables versus the iteration count k. Scaling coefficients: $\delta = 10^6$, $\alpha_{\varsigma,j} = 10^6$ and $\gamma_{\varsigma,j} = 0$ for $\varsigma \in \{m, b\}$ and $j \in \{1, 2\}$, and $\delta_m = \delta_b = \delta_r = 1$.

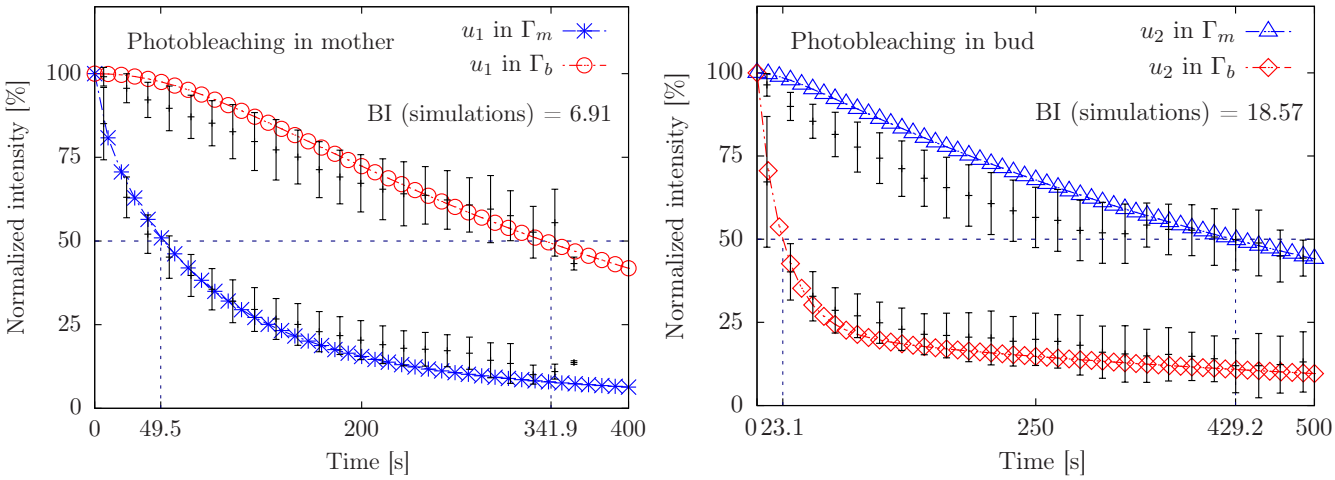

Figure 14: Example 4: Time evolution of the kinetics of fluorescence, obtained with the estimated optimal parameters, compared to the experimental data. (Left) Photobleaching applied to mother cortex. (Right) Photobleaching applied to the bud. Error bars indicate the standard deviation SD after averaging 20 different data measurements. Mean ± SD.

experimental data of the fluorescence signal at specific measurement times, along with its maximum and minimum values. It depicts a good agreement between the numerical results and the experimental measurements. In figures 10 and 12, we visualize the fluorescence intensity field for eight consecutive snapshots at the optimal state after applying a photobleaching to Γ_m and Γ_b, respectively. In both cases, the effect of the diffusion barrier at the bud neck region can be seen.

Remark that the estimated optimal control parameters satisfy $\mu_m^\star/\mu_b^\star \approx 1.0$ and $\mu_m^\star/\mu_r^\star \approx 21.2$. That is, the numerical results pinpoint that the diffusion of the reporter protein is similarly fast in the mother and in the bud compartments. However, it is 21 times slower in the barrier zone at the level of the bud neck. This is in agreement with the conclusions of many biologists that a physical diffusion barrier exists between the main compartments, whereas the protein Sec61-GF moves at similar speeds in the mother and bud compartments, see e.g. [Luedeke et al., 2005]. Consequently, the restricted diffusion in the bud neck region helps to slow the loss of fluorescence in the unbleached compartment in each FLIP experiments. From a biological point of view, the bud neck area features a specific morphology and contributes primarily, and among other things, to the retention of damage and aging factors between the mother and daughter cell, as mentioned above. Although our numerical study is in quantitative agreement with the diffusion barrier theory, we are still far from a high-fidelity mathematical description characterizing the intrinsic processes underlying such barriers.

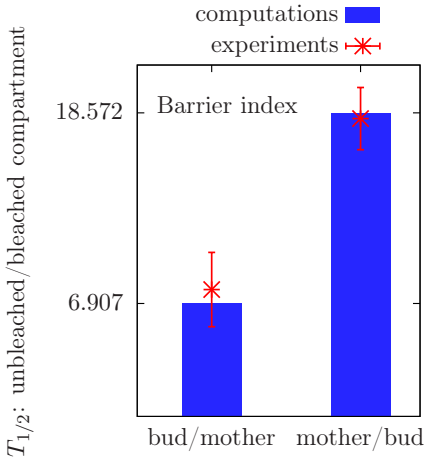

Figure 15: Example 4: Bar chart representing the $T_{1/2}$ of the unbleached compartment over the $T_{1/2}$ of the bleached compartment in the experimented in comparison to the simulated data. Mean ± SD.

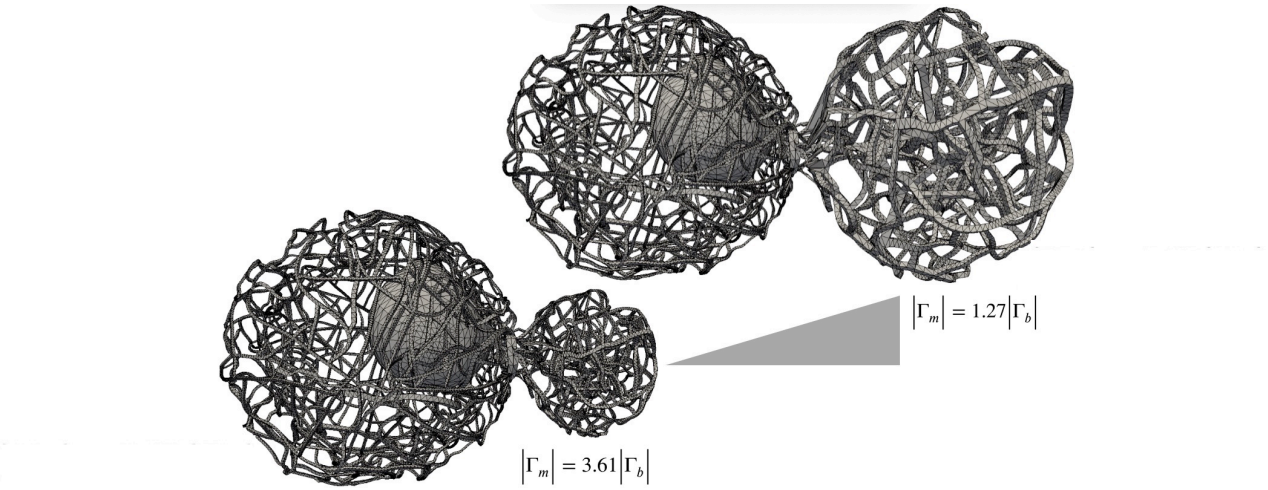

Figure 16: Example 4: (Left) ER mesh featuring a size of the bud nearly identical to the size of the mother cell. (Right) Segmented realistic realistic geometry of the yeast ER.

4.4 Example 4: Barrier index and dependence on compartment size ratio

Last but not least, we explore the effect of the compartment size on the kinetics of fluorescence. An index of great importance to biologists is the Barrier Index, referred to as BI. We first define $T_{1/2}$ as the time corresponding to a concentration equal to 50% of the initial concentration before photobleaching in a given compartment, as shown graphically in Fig 14. The BI represents the ratio of the times required to lose 50% of the fluorescence signal in the unbleached compartment compared to the bleached compartment.

An agreement in the calculation of the barrier index between the photobleached and unbleached compartments between the numerical and experimental results is obtained. Remark that the BI reaches much higher values (18.22 ± 1.90 experimentally and 18.572 numerically) when photobleaching is applied to the bud than when it is applied to the mother (7.76 ± 2.27 experimentally and 6.907 numerically), see Fig 15. The biologists rationalized that this might simply be due to the fact that the ER volume in the bud is smaller than that in the mother cell, leading to a much more rapid depletion of the smaller compartment upon FLIP.

In order to test whether this explanation indeed explains the yeast observations, the dependence between the compartment size ratio and the barrier index is studied numerically. We calculate how the observed BI would change when the relative volume of mother and bud is allowed to vary. Using the segmented ER geometry, we generate different meshes without changing the ER organization in the mother cortex but where the bud is increasingly bigger, until reaching almost the size of the mother compartment, see Fig 16. The surface meshes are subsequently remeshed in order to optimize the quality of the mesh for carrying out finite element calculations.

We consider the optimal parameters $\mu_m^\star$, $\mu_b^\star$ and $\mu_r^\star$ found previously. Parallel FLIP experiments were then simulated in each of these meshes, FLIPing either the mother or the bud compartment. In each geometry, the values of the BI obtained by photobleaching in the mother and in the bud are then compared. Whereas the ratio between the BI in the bud divided by the BI in the mother is high as long as the bud domain is significantly smaller than the mother cell, this ratio becomes close to 1 as the size of the bud approaches the size of the mother, see Fig. 17. A noticeable consequence is that, at least in budding yeast cell, the difference in BI depending on the place of photobleaching reflects the fact that (i) the ER membrane is compartmentalized and (ii) one compartment is smaller than the other.

5 Conclusions

This contribution presents a numerical framework for the modeling of the kinetics of fluorescently tagged molecules on the endoplasmic reticulum in asymmetrically dividing yeast cell. Using the Fluorescence Loss In Photobleaching technique, experiments are carried out in laboratory and provide measurement data on the decrease in the level of

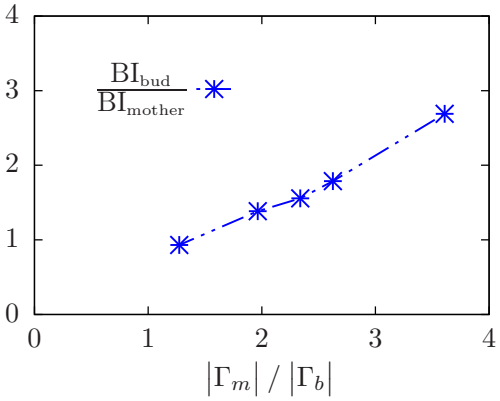

Figure 17: Example 4: Change in the ratio $\mathrm{BI}_{\mathrm{bud}}/\mathrm{BI}_{\mathrm{mother}}$ when the size of the bud increases relative to the size of the mother. It tends to 1 for similar sizes of ER compartments.

fluorescence in the different cellular compartments. To study the anisotropic molecular diffusion, we present a data-driven mathematical model based on the use of partial differential equations constrained optimization. Optimality conditions are derived and a gradient descent algorithm is used to estimate the diffusion parameters in the different cellular compartments. We address the main features of the method and we provide simulations with the aim of providing numerical evidence of compartmentalization in the ER membrane. Our computational model supports some biological conclusions indicating that the exchange of membrane proteins between mother and bud compartments is very slow, almost 20 times slower, compared to the diffusion of proteins into each compartment due to some surface diffusion limitations at the bud-neck zone.

This compartmentalization is also conserved in a broad range of cellular contexts, such as mouse neural stem cells and the early C. Elegans embryo, and contributes to processes as diverse as the confinement of protein aggregates during aging and the patterning of developing embryos. Further improvements are needed to better explore the compartmentalization in budding cells, while accounting for high fidelity mathematical descriptions. This is part of an ongoing work to explore concordant hypotheses for anisotropic exchange of ER proteins in yeast and and other cells [Laadhari et al., 2013, Laadhari, 2011], with more accurate mathematical formalism accounting for uncertainty quantification in the solution and the sensitivity of data noise on model parameters.

Acknowledgement

Conflict of interest

The authors declare no potential conflict of interests.

References

[Astorino et al., 2012] Astorino, M., Hamers, J., Shadden, S. C., and Gerbeau, J.-F. (2012). A robust and efficient valve model based on resistive immersed surfaces. *International Journal for Numerical Methods in Biomedical Engineering*, 28(9):937–959.

[Becker and Vexler, 2007] Becker, R. and Vexler, B. (2007). Optimal control of the convection-diffusion equation using stabilized finite element methods. *Numerische Mathematik*, 106(3):349–367.

[Betts, 2020] Betts, J. T. (2020). Practical methods for optimal control using nonlinear programming, third edition. *Society for Industrial and Applied Mathematics*.

[Casas et al., 2008] Casas, E., De Los Reyes, J. C., and Tröltzsch, F. (2008). Sufficient second-order optimality conditions for semilinear control problems with pointwise state constraints. *SIAM Journal on Optimization*, 19(2):616–643.

[Caudron and Barral, 2009] Caudron, F. and Barral, Y. (2009). Septins and the lateral compartmentalization of eukaryotic membranes. *Developmental Cell*, 16(4):493–506.

[Clay et al., 2014] Clay, L., Caudron, F., Denoth-Lippuner, A., Boettcher, B., Buvelot Frei, S., Snapp, E. L., and Barral, Y. (2014). A sphingolipid-dependent diffusion barrier confines er stress to the yeast mother cell. *eLife*, 3:e01883.

[Dayel et al., 1999] Dayel, M., F, H. E., and Verkman, A. S. (1999). Diffusion of green fluorescent protein in the aqueous-phase lumen of endoplasmic reticulum. *Biophysical Journal*, 76(5):2843–2851.

[Deckelnick et al., 2010] Deckelnick, K., Dziuk, G., Elliott, C. M., and Heine, C.-J. (2010). An h-narrow band finite-element method for elliptic equations on implicit surfaces. *IMA Journal of Numerical Analysis*, 30(2):351–376.

[Douglas and Russell, 1982] Douglas, Jr., J. and Russell, T. F. (1982). Numerical methods for convection-dominated diffusion problems based on combining the method of characteristics with finite element or finite difference procedures. *SIAM Journal on Numerical Analysis*, 19(5):871–885.

[Engl et al., 2000] Engl, H. W., Hanke, M., and Neubauer, A. (2000). *Regularization of Inverse Problems*. Mathematics and Its Applications, Springer Dordrecht, 1 edition. Volume 375, ISBN 978-0-7923-6140-4.

[English and Voeltz, 2013] English, A. and Voeltz, G. (2013). Endoplasmic reticulum structure and interconnections with other organelles. *Cold Spring Harbor Perspectives in Biology*, 5:a013227.

[Garvie and Trenchea, 2007] Garvie, M. R. and Trenchea, C. (2007). Optimal control of a Nutrient-Phytoplankton-Zooplankton-Fish system. *SIAM Journal on Control and Optimization*, 46(3):775–791.

[Garvie and Trenchea, 2014] Garvie, M. R. and Trenchea, C. (2014). Identification of space-time distributed parameters in the gierer–meinhardt reaction-diffusion system. *SIAM Journal on Applied Mathematics*, 74(1):147–166.

[Gunzburger, 2002] Gunzburger, M. D. (2002). Perspectives in flow control and optimization. *Society for Industrial and Applied Mathematics*.

[Hogea et al., 2008] Hogea, C., Davatzikos, C., and Biros, G. (2008). An image-driven parameter estimation problem for a reaction–diffusion glioma growth model with mass effects. *Journal of Mathematical Biology*, 56(6):793–825.

[Hollis et al., 1987] Hollis, S. L., Martin, Jr., R. H., and Pierre, M. (1987). Global existence and boundedness in reaction-diffusion systems. *SIAM Journal on Mathematical Analysis*, 18(3):744–761.

[Hoppe and Neitzel, 2022] Hoppe, F. and Neitzel, I. (2022). Optimal control of quasilinear parabolic pdes with state-constraints. *SIAM Journal on Control and Optimization*, 60(1):330–354.

[Janela, J et al., 2005] Janela, J, Lefebvre, A, and Maury, B (2005). A penalty method for the simulation of fluid - rigid body interaction. *ESAIM: Proc.*, 14:115–123.

[Jiang and Zhang, 2000] Jiang, C. S. and Zhang, Y. X. (2000). A parameter identification and inversion method for a class of reaction-diffusion systems. *Control Theory Appl.*, 17:193 – 197.

[Kelley, 1999] Kelley, C. T. (1999). Iterative methods for optimization. *Society for Industrial and Applied Mathematics*.

[Khaksar-E Oshagh and Shamsi, 2017] Khaksar-E Oshagh, M. and Shamsi, M. (2017). Direct pseudo-spectral method for optimal control of obstacle problem – an optimal control problem governed by elliptic variational inequality. *Mathematical Methods in the Applied Sciences*, 40(13):4993–5004.

[Kim and Park, 2008] Kim, D. and Park, E.-J. (2008). A posteriori error estimators for the upstream weighting mixed methods for convection diffusion problems. *Computer Methods in Applied Mechanics and Engineering*, 197(6):806–820.

[Laadhari, 2011] Laadhari, A. (2011). Numerical modelling of the dynamics of red blood cells using the level set method. *HAL, Université de Grenoble*, 2011(0). URL: https://tel.archives-ouvertes.fr/tel-00598251.

[Laadhari, 2017] Laadhari, A. (2017). Exact newton method with third-order convergence to model the dynamics of bubbles in incompressible flow. *Applied Mathematics Letters*, 69:138–145.

[Laadhari, 2018a] Laadhari, A. (2018a). Implicit finite element methodology for the numerical modeling of incompressible two-fluid flows with moving hyperelastic interface. *Applied Mathematics and Computation*, 333:376–400.

[Laadhari, 2018b] Laadhari, A. (2018b). An operator splitting strategy for fluid-structure interaction problems with thin elastic structures in an incompressible newtonian flow. *Applied Mathematics Letters*, 81:35–43.

[Laadhari and Quarteroni, 2016] Laadhari, A. and Quarteroni, A. (2016). Numerical modeling of heart valves using resistive eulerian surfaces. *International Journal for Numerical Methods in Biomedical Engineering*, 32(5):e02743. e02743 cnm.2743.

[Laadhari et al., 2013] Laadhari, A., Ruiz-Baier, R., and Quarteroni, A. (2013). Fully eulerian finite element approximation of a fluid-structure interaction problem in cardiac cells. *International Journal for Numerical Methods in Engineering*, 96(11):712–738.

[Laadhari and Székely, 2017] Laadhari, A. and Székely, G. (2017). Eulerian finite element method for the numerical modeling of fluid dynamics of natural and pathological aortic valves. *Journal of Computational and Applied Mathematics*, 319:236–261.

[Laadhari and Székely, 2017] Laadhari, A. and Székely, G. (2017). Fully implicit finite element method for the modeling of free surface flows with surface tension effect. *Int J Numer Meth Biomed Engng*, 111(11):1047–1074.

[Lenhart and Workman, 2007] Lenhart, S. and Workman, J. T. (2007). Optimal control applied to biological models (1st ed.). *Mathematical and Computational Biology Series, Chapman and Hall/CRC*.

[Liao et al., 2008] Liao, G. G., Cai, X., Fleitas, D., Luo, X., Wang, J., and Xue, J. (2008). Optimal control approach to data set alignment. *Applied Mathematics Letters*, 21(9):898–905.

[Lippencott-Schwartz et al., 2003] Lippencott-Schwartz, J., Altan-Bonnet, N., and Patterson, G. H. (2003). Photobleaching and photoactivation: following protein dynamics in living cells. *Nature Cell Biology*, 5:S7–S14.

[Lippincott-Schwartz et al., 2001] Lippincott-Schwartz, J., Snapp, E., and Kenworthy, A. (2001). Studying protein dynamics in living cells. *Nature Reviews Molecular Cell Biology*, 2(6):444–456.

[Luedeke et al., 2005] Luedeke, C., Frei, S. B., Sbalzarini, I., Schwarz, H., Spang, A., and Barral, Y. (2005). Septin-dependent compartmentalization of the endoplasmic reticulum during yeast polarized growth. *Journal of Cell Biology*, 169(6):897–908.

[Martínez et al., 2000] Martínez, A., Rodríguez, C., and Vázquez-Méndez, M. E. (2000). Theoretical and numerical analysis of an optimal control problem related to wastewater treatment. *SIAM Journal on Control and Optimization*, 38(5):1534–1553.

[Mills, 1983] Mills, W. H. (1983). Algorithmic methods in optimal control (w. a. gruver and e. sach). *Society for Industrial and Applied Mathematics, SIAM Review*, 25(4):579–580.

[Moor, 1967] Moor, H. (1967). Endoplasmic reticulum as the initiator of bud formation in yeast (s. cerevisiae). *Archiv für Mikrobiologie*, 57(2):135–146.

[Perić and Owen, 1992] Perić, D. and Owen, D. R. J. (1992). Computational model for 3-D contact problems with friction based on the penalty method. *International Journal for Numerical Methods in Engineering*, 35(6):1289–1309.

[Puhka et al., 2007] Puhka, M., Vihinen, H., Joensuu, M., and Jokitalo, E. (2007). Endoplasmic reticulum remains continuous and undergoes sheet-to-tubule transformation during cell division in mammalian cells. *Journal of Cell Biology*, 179(5):895–909.

[Ruo et al., 2002] Ruo, L., Wenbin, L., Heping, M., and Tao, T. (2002). Adaptive finite element approximation for distributed elliptic optimal control problems. *SIAM Journal on Control and Optimization*, 41(5):1321–1349.

[Saramito, 2020] Saramito, P. (2020). *Efficient C++ Finite Element computing with Rheolef*. CNRS-CCSD ed., Grenoble, France. HAL version: v15. Accessed: 26.09.22.

[Shcheprova et al., 2008] Shcheprova, Z., Baldi, S., Frei, S., Gonnet, G., and Barral, Y. (2008). A mechanism for asymmetric segregation of age during yeast budding. *Nature*, 454(7205):728–734.

[Tabas and Ron, 2011] Tabas, I. and Ron, D. (2011). Integrating the mechanisms of apoptosis induced by endoplasmic reticulum stress. *Nature Cell Biology*, 13(3):184–190.

[Tikhonov et al., 1995] Tikhonov, K. A. N., Goncharsky, A. V., Stepanov, V. V., and Yagola, A. G. (1995). *Numerical Methods for the Solution of Ill-Posed Problems*, volume 328. Mathematics and Its Applications. Springer Dordrecht. https://doi.org/10.1007/978-94-015-8480-7.

[Vogel, 2002] Vogel, C. R. (2002). Computational methods for inverse problems. *Society for Industrial and Applied Mathematics*.

[West et al., 2011] West, M., Zurek, N., Hoenger, A., and Voeltz, G. K. (2011). A 3d analysis of yeast er structure reveals how er domains are organized by membrane curvature. *The Journal of cell biology*, 132(2):333–346.

[Yan and Zhou, 2008] Yan, N. and Zhou, Z. (2008). A priori and a posteriori error estimates of streamline diffusion finite element method for optimal control problem governed by convection dominated diffusion equation. *Numerical Mathematics: Theory, Methods and Applications*, 1(3):297–320.

[Yan and Zhou, 2009] Yan, N. and Zhou, Z. (2009). A priori and a posteriori error analysis of edge stabilization galerkin method for the optimal control problem governed by convection-dominated diffusion equation. *Journal of Computational and Applied Mathematics*, 223(1):198–217.

[Yücel et al., 2015] Yücel, H., Stoll, M., and Benner, P. (2015). A discontinuous galerkin method for optimal control problems governed by a system of convection-diffusion pdes with nonlinear reaction terms. *Computers and Mathematics with Applications*, 70(10):2414–2431.

[Zhou and Yan, 2010] Zhou, Z. and Yan, N. (2010). The local discontinuous galerkin method for optimal control problem governed by convection diffusion equations. *International Journal of Numerical Analysis and Modeling*, 7(4):681–699.

[Zhu and Zeng, 2003] Zhu, J. and Zeng, Q. (2003). A mathematical formulation for optimal control of air pollution. *Science in China Series D: Earth Sciences*, 46(10):994–1002.